Cell Reports

Article

Fyn Kinase Controls Tau Aggregation *In Vivo*

Graphical Abstract

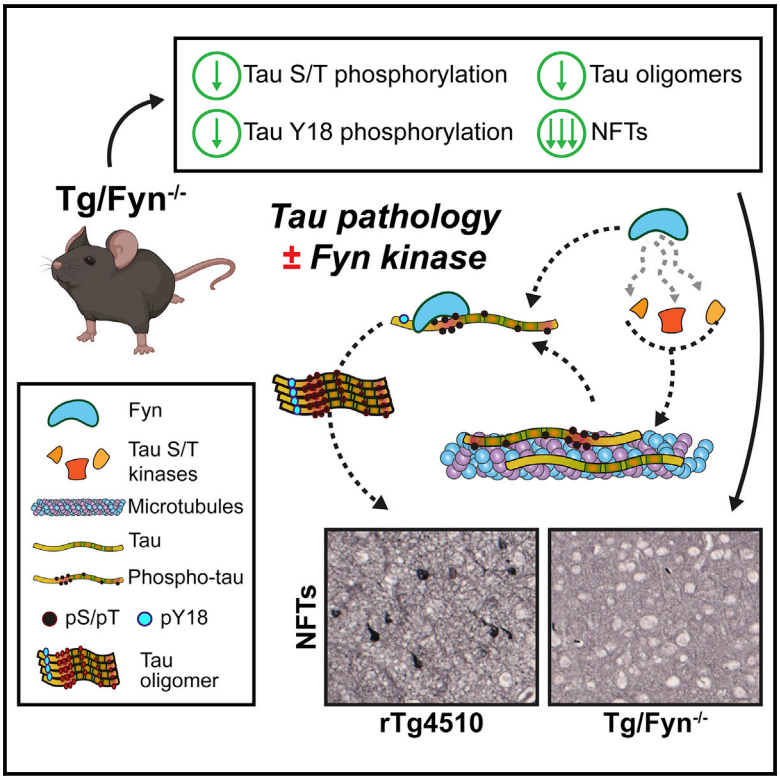

Highlights

- Tau transgenic mice without Fyn (Tg/Fyn$^{-/-}$) exhibit near-complete ablation of NFTs
- Tg/Fyn$^{-/-}$ mice show altered tau hyperphosphorylation, solubility, and accumulation
- Tg/Fyn$^{-/-}$ brain lysates induce alternative tau conformers in tau biosensor cells
- Tau's *in vitro* fibrillization is controlled by the Fyn epitope tyrosine 18

Authors

Adam Briner, Jürgen Götz, Juan Carlos Polanco

Correspondence

j.polanco@uq.edu.au

In Brief

Briner et al. present Fyn as a regulator of tau pathology. Tau transgenic mice lacking Fyn exhibit reduced phosphorylation of tau at several pathological residues, reduced tau oligomer formation, and a near-complete ablation of neurofibrillary tangles. Targeting Fyn represents a therapeutic strategy for Alzheimer's disease and other tauopathies.

Briner et al., 2020, Cell Reports *32*, 108045
August 18, 2020
https://doi.org/10.1016/j.celrep.2020.108045

CellPress

Cell Reports

CellPress
OPEN ACCESS

Article

Fyn Kinase Controls Tau Aggregation *In Vivo*

Adam Briner,[1] Jürgen Götz,[1] and Juan Carlos Polanco[1,2,*]
[1]Clem Jones Centre for Ageing Dementia Research (CJCADR), Queensland Brain Institute (QBI), The University of Queensland, Brisbane, QLD 4072, Australia
[2]Lead Contact
*Correspondence: j.polanco@uq.edu.au
https://doi.org/10.1016/j.celrep.2020.108045

SUMMARY

Alzheimer's disease (AD) is a proteinopathy exhibiting aggregation of β-amyloid (Aβ) as amyloid plaques and tau as neurofibrillary tangles (NFTs), whereas primary tauopathies display only a tau pathology. Aβ toxicity is mediated by Fyn kinase in a tau-dependent process; however, whether Fyn controls tau pathology in diseases that lack Aβ pathology remains unexplored. To address this, we generate the Tg/Fyn$^{-/-}$ mouse, which couples mutant tau overexpression with Fyn knockout. Surprisingly, Tg/Fyn$^{-/-}$ mice exhibit a near-complete ablation of NFTs, alongside reduced tau hyperphosphorylation, altered tau solubility, and diminished synaptic tau accumulation. Furthermore, Tg/Fyn$^{-/-}$ brain lysates elicit less tau seeding in tau biosensor cells. Lastly, the fibrillization of tau is boosted by its pseudophosphorylation at the Fyn epitope Y18. Together, this identifies Fyn as a key regulator of tau pathology independently of Aβ-induced toxicity and thereby represents a potentially valuable therapeutic target for not only AD but also tauopathies more generally.

INTRODUCTION

Protein aggregation is a defining feature of all neurodegenerative disorders. Affecting more than 50 million people worldwide, Alzheimer's disease (AD) is the most prevalent form of dementia (Polanco et al., 2018a). AD is a proteinopathy characterized by two histopathological lesions: extracellular amyloid plaques consisting of aggregated β-amyloid (Aβ) peptides and neurofibrillary tangles (NFTs) consisting of the microtubule-associated protein tau within the somatodendritic domain of neurons. Aβ and tau act synergistically in impairing neuronal and synaptic functions (Polanco et al., 2018a). However, to date, the signaling pathways that underlie this toxic cascade remain incompletely understood.

Tau is an intrinsically disordered and highly soluble, axonally enriched protein that in its longest human isoform has 80 serine and threonine residues and 5 tyrosine residues, which can potentially be phosphorylated (Wang and Mandelkow, 2016). In disease, tau becomes abnormally hyperphosphorylated at specific sites (Grundke-Iqbal et al., 1986), which reduces its affinity for its primary ligand tubulin (Biernat et al., 1993) and promotes its accumulation in the somatodendritic compartment (Hoover et al., 2010; Xia et al., 2015). Multiple factors, including (but not limited to) specific phosphorylation patterns (Despres et al., 2017), interactions with other proteins (Apicco et al., 2018; Shelton et al., 2017), and templated prion-like misfolding (Clavaguera et al., 2013; Mirbaha et al., 2018; Sanders et al., 2014), combine to drive its oligomerization. Eventually, these tau oligomers fibrillize and undergo a phase transition from the soluble to the insoluble state, finally depositing as NFTs (Wegmann et al., 2018). It appears that tau is particularly neurotoxic in its soluble, oligomeric form (Fá et al., 2016; Lasagna-Reeves et al., 2011) and that this tau species is capable of propagating from neuron to neuron, a phenomenon that is thought to underlie the stereotyped spreading of tau pathology in the diseased human brain (Polanco et al., 2018b, 2016; Takeda et al., 2015).

Several lines of evidence support a central role for tau in AD pathogenesis and neurodegeneration. These include the fact that tau is capable of causing neurodegeneration by itself, as evidenced by familial tauopathies (such as frontotemporal lobar degeneration [FTLD] with tau) (Forrest et al., 2018; Hutton et al., 1998), as well as other sporadic tauopathies (Li et al., 2019). Furthermore, the severity and duration of AD correlates with the gradual region-to-region spreading of NFTs, but not that of amyloid plaque deposition (Nelson et al., 2012). Moreover, tau and not Aβ pathology is the predominant cause of neuronal silencing in animal models of AD (Busche et al., 2019). Lastly, there is accumulating evidence that postsynaptic Aβ-initiated synaptic dysfunction is dependent on tau (Götz et al., 2001; Ittner et al., 2010; Roberson et al., 2007).

A crucial mediator of this tau-dependent, Aβ-initiated synaptic toxicity is the Src family non-receptor tyrosine kinase Fyn. Fyn is a central hub for N-methyl D-aspartate receptor (NMDAR) signaling and a key enzyme in synaptic plasticity and long-term potentiation (Grant et al., 1992; Trepanier et al., 2012). Initial interest in Fyn in an AD framework came from the observation that Fyn levels rise in AD (Ho et al., 2005), and that the enzyme regulates the synaptic deficits elicited by Aβ; Fyn overexpression exacerbates cognitive defects and loss of synapses in Aβ-forming transgenic mice (Chin et al., 2005), while genetic Fyn depletion or inhibition protects from Aβ-induced cell death and memory deficits (Chin et al., 2004; Kaufman et al., 2015; Lambert et al., 1998). Critically, Fyn physically interacts with tau through its SH2 and SH3 domains (Bhaskar et al., 2005; Lau et al.,

2016; Lee et al., 1998; Usardi et al., 2011) and directly phosphorylates tau at residue Y18 (Bhaskar et al., 2010; Lee et al., 2004), an event that enhances the affinity of Fyn for tau and mirrors the progression of tauopathy in humans and tau transgenic mice (Bhaskar et al., 2010; Neddens et al., 2018).

Mechanistic insight into the pathological basis of the tau-Fyn interaction was provided by the demonstration that tau's targeting of Fyn to the postsynapse facilitates Aβ neurotoxicity by stabilizing the coupling of NMDARs with PSD95 (Ittner et al., 2010). Additional neuronal pathways of Aβ-induced synaptic dysfunction involving the tau-Fyn axis have since been reported (Frandemiche et al., 2014; Larson et al., 2012; Nygaard, 2018; Um et al., 2012, 2013). Furthermore, the phosphorylation of tau at Y18 by Fyn specifically appears to aid the targeting of tau to the postsynapse (Larson et al., 2012; Usardi et al., 2011), where pY18-tau is capable of inducing excitotoxic NMDAR activity even without binding Fyn directly (Miyamoto et al., 2017). Additional evidence for the importance of the tau-Fyn interaction in AD comes from the recent discovery that these proteins jointly boost the mislocalization and hyperphosphorylation of tau through the Aβ-induced activation of the ERK/S6 pathway, thereby causing local *de novo* translation of tau in the somatodendritic compartment (Li and Götz, 2017).

Although the shared pathways of tau and Fyn in Aβ signaling have been extensively investigated, to our knowledge, there are no studies that have examined how Fyn itself influences tau aggregation in a system that lacks Aβ. We therefore generated the Tg/Fyn$^{-/-}$ transgenic mouse strain in which FTLD-associated mutant tau overexpression is coupled with a Fyn knockout.

To our surprise, these mice exhibited a remarkable reduction in NFT formation, reduced tau histopathology with respect to multiple tau phosphoepitopes, altered tau solubility, and decreased synaptic accumulation of tau. Furthermore, using a tau biosensor cell line, we showed that Tg/Fyn$^{-/-}$ brain lysates seed fewer tau aggregates, which are more fragmented and disordered than those induced with rTg4510 lysates. Finally, our results revealed that tau fibrillization is accelerated by the phosphorylation of tau at Y18. Together, these findings lead us to conclude that Fyn is essential in mediating the formation of high-molecular-weight tau aggregates and thereby drives tau pathology independently of Aβ.

RESULTS

The Novel Mouse Strain Tg/Fyn$^{-/-}$ Exhibits a Near-Complete Loss of Cortical NFTs

In order to understand the function of Fyn in the development of tau pathology, we crossed the tauopathy model rTg4510 (that expresses P301L FTLD mutant tau) with a mouse with a complete knockout of the kinase Fyn, generating a new strain that we named Tg/Fyn$^{-/-}$.

We first sought to evaluate the degree of neurofibrillary tau pathology in the Tg/Fyn$^{-/-}$ strain relative to the parental rTg4510 strain by using Gallyas silver staining to detect argyrophilic tau inclusions (Figure 1). Three neocortical optical fields were used in this analysis (Figure 1N): the dorsal neocortex, comprising retrosplenial and parietal association areas (Figures 1A–1D); the somatosensory cortex, comprising regions S1 and S2 (Figures 1E–1H); and the temporal neocortex, comprising the temporal association area and ectorhinal cortex (Figures 1I–1L). For each region, the number of NFTs per field was reported, together with a combined total for the entire neocortex (Figure 1M). NFTs were not quantified in the hippocampal formation due to their relative sparsity in rTg4510 mice at 6 months of age, when the analysis was performed.

As previously reported (Santacruz et al., 2005), the rTg4510 mice presented with pronounced cortical NFT accumulation. Strikingly, however, Tg/Fyn$^{-/-}$ mice displayed a near-complete abolishment of neocortical NFTs, with reductions relative to rTg4510 NFT counts of ~90% in the dorsal neocortex, 94% in the somatosensory cortex, and 96% in the temporal neocortex, amounting to an overall mean cortical decrease of 94%.

Despite their tight correlation with disease progression, it has been suggested that NFTs themselves may be benign and inactive with respect to eliciting neuronal toxicity and that aggregation-intermediary soluble tau oligomers are in fact the most neurotoxic tau species (Kuchibhotla et al., 2014; Lasagna-Reeves et al., 2011). Accordingly, the strong reduction in NFT burden was complemented by a significant 58% reduction in tau oligomers as assessed by dot-blot analysis of PBS brain lysates using the tau-oligomer-specific antibody TOC1 (Figures 1O and 1P). Thus, Tg/Fyn$^{-/-}$ mice display a delay in the appearance and progression of the hallmark aggregated species in tauopathy.

Given the strong reduction in tau pathology in the Tg/Fyn$^{-/-}$ mice, we next investigated their spatial memory with a 6-day active place avoidance paradigm, revealing no recuperation of the memory defects observed in the parent rTg4510 strain (Figure S1A–S1E). Analysis of baseline locomotion and anxiety-like phenotypes using open-field activity monitors similarly revealed no alterations in Tg/Fyn$^{-/-}$ behavior relative to rTg4510 (Figures S1F–S1H), and measurement of coordination and equilibrium using an accelerating Rotarod revealed no significant differences between wild type (WT) and either transgenic strain (Figure S1I). Interestingly, Tg/Fyn$^{-/-}$ mice displayed a slight yet significant reduction in brain mass (Figure S1J). This may reflect the fact that Fyn-knockout animals exhibit altered neural development and myelination (Umemori et al., 1994), abnormal electrophysiological profiles, reduced long-term potentiation, and impaired spatial memory (Grant et al., 1992; Kojima et al., 1997). Furthermore, recent findings have shown that neurodegeneration in rTg4510 mice may result from a major deletion in the *Fgf14* locus that is, at least to some degree, independent of tau pathology (Gamache et al., 2019; Goodwin et al., 2019).

Fyn performs well-characterized roles in mediating inflammatory signaling pathways in astrocytes and microglia (Lee et al., 2017; Panicker et al., 2015), and hyperactivation of these cell types correlates with increased tau pathology and contributes to disease progression (Asai et al., 2015; Laurent et al., 2018; Narasimhan et al., 2017). However, we also found that the amelioration of NFT burden in Tg/Fyn$^{-/-}$ mice was not accompanied by a reduction in glial activation compared to the parental rTg4510 strain (Figure S2), suggesting that the reduction in tau aggregation is unlikely due to a global decrease in neuroinflammation and rather is mediated by Fyn through a neuronal

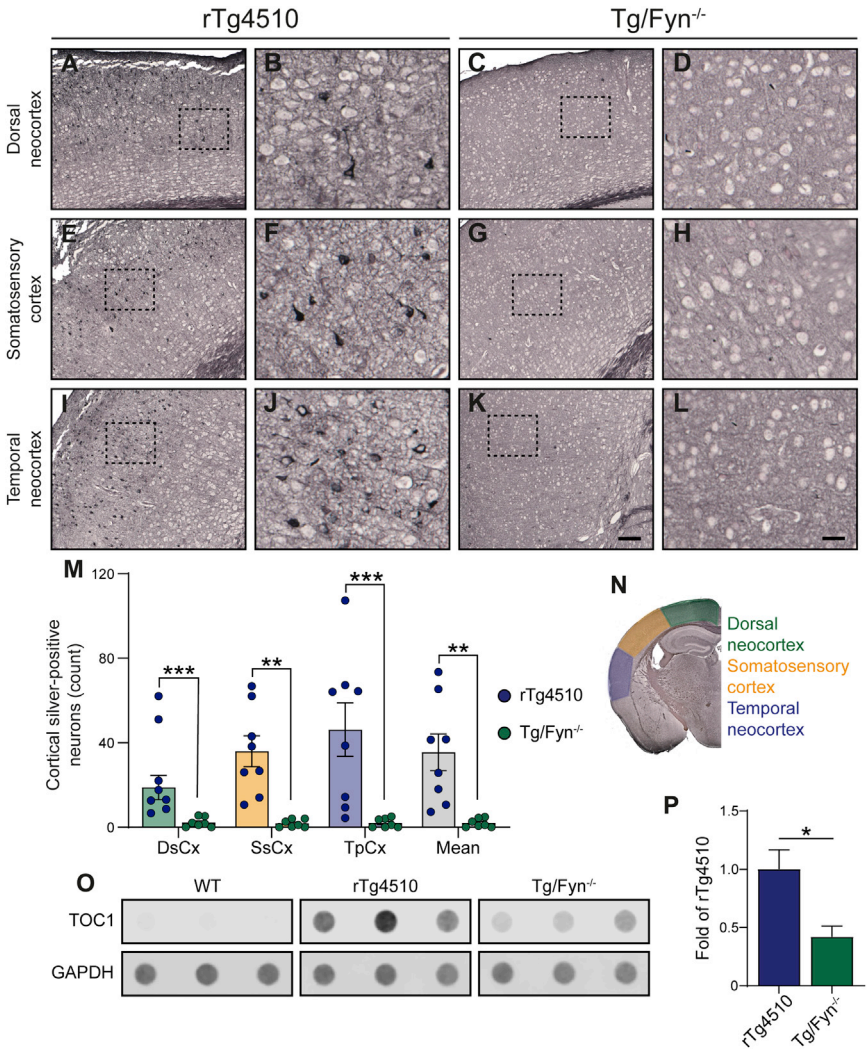

Figure 1. Tg/Fyn$^{-/-}$ Mice Exhibit a Near-Complete Ablation of Cortical NFTs and Reduced Tau Oligomer Levels

(A–L) Representative images of Gallyas-stained silver-positive NFTs in 6-month-old rTg4510 and Tg/Fyn$^{-/-}$ mice. NFTs were manually counted in three neocortical regions, as outlined in (N): dorsal neocortex (DsCx), comprising retrosplenial and parietal association areas (A–D); somatosensory cortex (SsCx), comprising regions S1 and S2 (E–H); and temporal neocortex (TpCx), comprising the temporal association area and ectorhinal cortex (I–L). High-magnification images are presented in (B), (D), (F), (H), (J), and (L). Scale bars represent 100 μm (K) and 25 μm (L).

(M) Quantification of cortical silver-positive neurons counts for each neocortical region with the mean across the three regions graphed alongside. Data represent mean ± SEM; n = 8 for rTg4510 mice and n = 7 for Tg/Fyn$^{-/-}$ mice. *p < 0.05, **p < 0.01, and ***p < 0.001 (t test).

(O) WT, rTg4510, and Tg/Fyn$^{-/-}$ PBS-soluble brain lysates, generated with low-speed centrifugation to preserve tau oligomers, were probed by dot blot with the anti-oligomeric tau antibody TOC1. GAPDH was utilized as a loading control.

(P) Quantification of (O). Data are presented as mean ± SEM; n = 3 mice. *p < 0.05 (one-way ANOVA with Holm-Sidak's multiple comparisons test).

mechanism. However, as outlined above, care must be taken when interpreting these results due to the large genomic alterations present in the parental rTg4510 strain.

Based on these data, we focused our subsequent analyses on the histological and biochemical aspects of tau aggregation in our novel strain.

Phosphorylation of Tau at Y18 Is Reduced in Tg/Fyn$^{-/-}$ Mice

Fyn phosphorylates tau directly at residue Y18 (pY18), an epitope that is present early in the progression of human FTLD (Neddens et al., 2018), as well as in mice overexpressing P301L tau (Bhaskar et al., 2010; Lee et al., 2004). Moreover, pY18 has been shown to facilitate the targeting of tau to dendritic spines through its interaction with the SH2 domain of Fyn (Usardi et al., 2011). More recently, pY18-tau has been shown to be capable of mediating excitotoxic NMDAR Ca^{2+} influx in cultured neurons (Miyamoto et al., 2017). Because of the apparent etiological importance of this phosphoepitope, we evaluated the localization and prevalence of pY18 tau in Tg/Fyn$^{-/-}$ mice relative to the rTg4510 strain (Figure 2). Our analysis revealed that pY18 was modestly reduced in the Tg/Fyn$^{-/-}$ hippocampal formation (Figures 2A–2C and 2F–2H), with only the CA2/3 subregion presenting a significant decrease in integrated fluorescence intensity and percentage area of positive labeling (61% for the latter parameter, Figures 2C and 2H). Interestingly, the CA2/3 subregion of Tg/Fyn$^{-/-}$ mice presented a strong decrease of pY18 in the neuronal somas but a strong labeling of mossy fibers, a phenomenon that was notably inverse in rTg4510 mice (see arrowheads in Figures 2A and 2C), suggesting that Fyn kinase contributes to the somatic subcellular localization of pY18 tau. Both the somatosensory and temporal cortical regions exhibited strongly attenuated pY18 reactivity, resulting in a combined 56% mean neocortical reduction in pY18 staining (Figures 2D, 2E, and 2I–2K).

Morphologically, pY18 staining was largely restricted to the soma, and as such, it mirrored mature NFTs, with only a small proportion of CA1 (Figure 2B) and cortical neurons (Figures 2D–2E) in rTg4510 mice presenting with tau in dystrophic apical dendrites. However, this finding was never observed in Tg/Fyn$^{-/-}$ mice (Figures 2B, 2D, and 2E). The incomplete abolition of neuronal pY18 staining suggests the existence of alternative tau tyrosine kinases, which include the spleen tyrosine kinase Syk (Köhler et al., 2017) and the proline-rich tyrosine kinase Pyk2 (Li and Götz, 2018), and highlights the importance of this tau species in neuronal physiology.

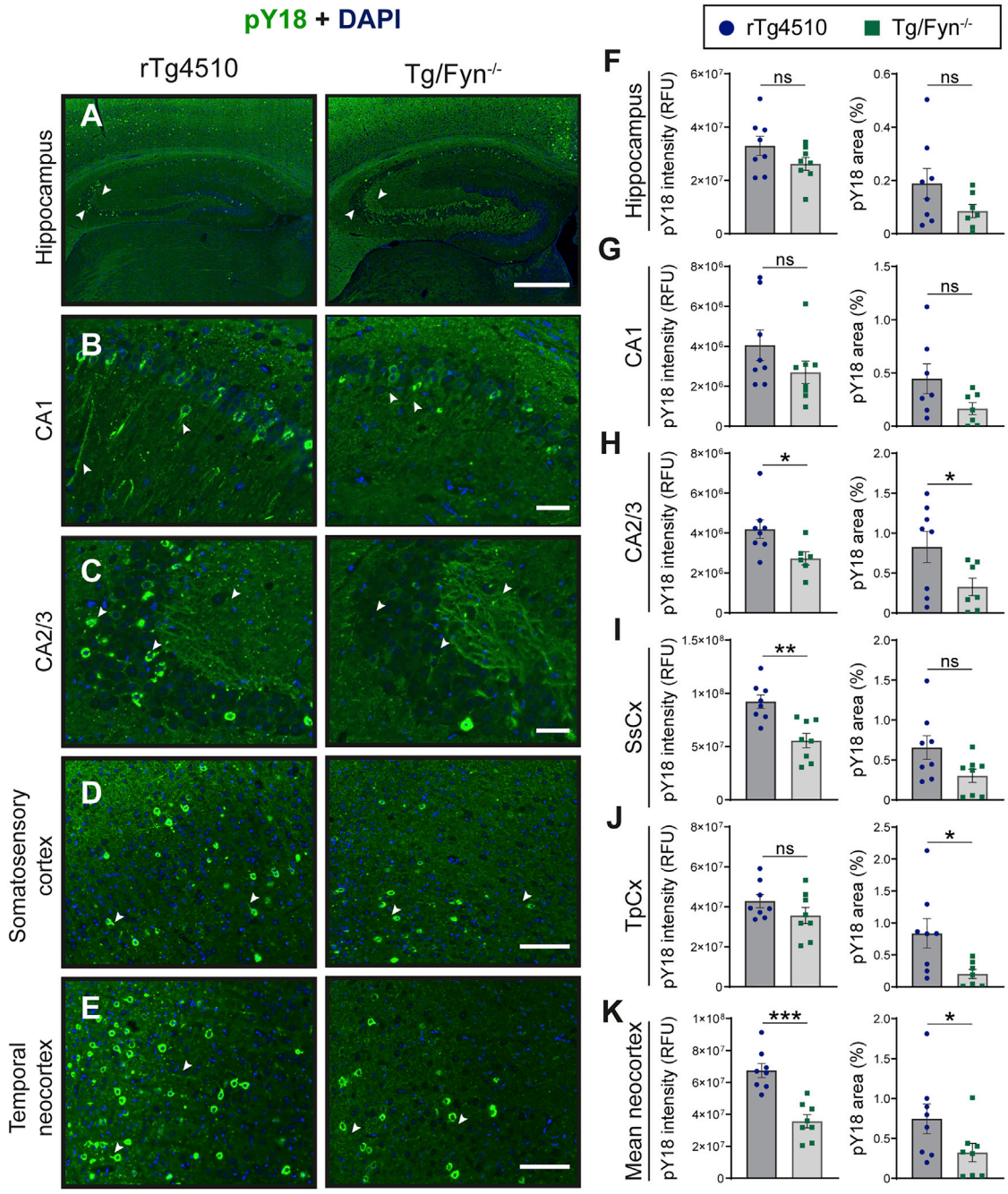

Figure 2. Neuronal pY18-Tau Immunolabeling Is Reduced in a Region-Dependent Manner in Tg/Fyn$^{-/-}$ Mice

(A–E) Representative images of pY18 immunofluorescence (green) with DAPI counterstaining for nuclei (blue) in hippocampal neurons. Arrowheads in (B), (D), and (E) indicate pY18 tau accumulations in the apical dendrites of rTg4510 mice that are largely absent in Tg/Fyn$^{-/-}$ mice. Arrowheads in (A) and (C) show somas and mossy fibers, with prominent mossy fiber pY18 labeling emanating from CA2/3 neurons in Tg/Fyn$^{-/-}$ but strongly decreased in the neuronal somas. Scale bars represent 500 μm (A), 50 μm (B and C), and 100 μm (D and E).

(F–K) Quantification of rTg4510 and Tg/Fyn$^{-/-}$ pY18 levels by integrated fluorescence signal and thresholded percentage area within the regions shown in (A) –(E). Data are presented as mean ± SEM; n = 8 for both genotypes in (I) and (J); for (F)–(H) and (K), n = 8 for rTg4510 mice and n = 7 for Tg/Fyn$^{-/-}$. *p < 0.05; **p < 0.01; ***p < 0.001; and ns, not significant (t test).

Tg/Fyn$^{-/-}$ Mice Display Region-Specific Reductions in Hyperphosphorylated Tau

We next sought to establish the amount of pathological, hyperphosphorylated tau present in 6-month-old Tg/Fyn$^{-/-}$ mice. Phosphorylation of specific serine and threonine residues of tau, in both humans and mice, correlates spatiotemporally with disease progression and can be used to stage the cytopathological status of tauopathy (Braak et al., 2006). In our study (Figure 3), we used antibodies directed at the pathological phosphoepitopes AT8 (pS202/pT205) and AT180 (pT231/pS235).

We found that AT8 labeling in the hippocampus as a whole was significantly reduced relative to that in rTg4510 mice (Figures 3B and 3M), with the CA2/3 subregion also exhibiting a similar decrease (Figures 3D and 3M). A nonsignificant reduction in the degree of positive labeling was observed for CA1 neurons (Figures 3C and 3M). AT8 staining was most predominantly diminished in the cortex, with a 39% decrease in percentage area of positive cellular labeling when averaged across two neocortical regions (Figures 3E, 3F, and 3M). Notably, AT8 phospho-tau was largely excluded from apical dendrites in the CA1 *stratum radiatum* and neocortical regions in Tg/Fyn$^{-/-}$ mice (Figures 3C, 3E, and 3F).

AT180 immunostaining revealed fewer differences between rTg4510 and Tg/Fyn$^{-/-}$ mice, with no significant decreases found in hippocampal formation (Figures 3H–3J and 3N). However, as for AT8, cortical AT180 positivity was significantly attenuated in Tg/Fyn$^{-/-}$ mice, where a mean 29% reduction was found (Figures 3K, 3L, and 3N). Notably, the Tg/Fyn$^{-/-}$ neuropil in both hippocampal and cortical regions exhibited decreased basal AT180 staining intensity (Figures 3I–3L and 3N), and as for AT8, the presence of AT180 phospho-tau in CA1 (Figure 3I) and cortical apical dendrites (Figures 3K and 3L) was reduced.

Overall, Tg/Fyn$^{-/-}$ mice displayed a phospho-tau phenotype characterized by reduced cortical AT8 and AT180 levels and an apparent decrease in the targeting of pathological tau to dendritic compartments. Combined with our analyses of NFT burden and pY18 labeling, these histological findings suggest that the Tg/Fyn$^{-/-}$ model displays an amelioration of tau pathology, particularly within the neocortex, with reduced accumulation of somatodendritic high-molecular-weight tau.

Tau Solubility Is Altered in Tg/Fyn$^{-/-}$ Mice

In solution, tau is a highly disordered protein with little secondary structure (Mukrasch et al., 2009). In disease, however, tau aggregates and oligomerizes, eventually undergoing a series of phase transitions to form structured, insoluble deposits. We therefore analyzed the relative solubility of tau in Tg/Fyn$^{-/-}$ mouse brains (Figure 4) using a series of pan- and phospho-tau-specific antibodies. WT, rTg4510, and Tg/Fyn$^{-/-}$ brains were serially fractionated to generate RAB-soluble (containing predominantly soluble tau) and RIPA/SDS-soluble (containing mostly insoluble, fibrillar tau) fractions (Figure 4A). These preparations were blotted and analyzed using the anti-tau antibodies Tau5 (total human and murine tau), HT7 (total human tau), AT8, AT180, and pY18.

In the RAB-soluble fraction, the amount of total Tau5, HT7, and pY18 tau in Tg/Fyn$^{-/-}$ brains was indistinguishable from that in rTg4510 brains (Figures 4B and 4D). Intriguingly, Tg/Fyn$^{-/-}$ AT8 and AT180 levels were strongly decreased (33% and 42%, respectively) from the levels observed in the rTg4510 brains, suggesting that phosphorylation of these sites precedes the biochemical conversion from the RAB- to the RIPA/SDS-soluble state, consistent with previous studies which show that these phosphoepitopes enhance the dissociation of tau from microtubules and prime it to aggregate (Despres et al., 2017). In agreement with our analysis of tau oligomers obtained with the TOC1 antibody, tau oligomers of ~150 kDa were strongly reduced in the Tg/Fyn$^{-/-}$ RAB-soluble fraction (Figure S3).

Conversely, strong decreases from rTg4510 levels were observed for all analyzed total and phospho-tau markers in the RIPA/SDS-soluble fraction of Tg/Fyn$^{-/-}$ brains, with 33% for Tau5, 20% for HT7, 52% for AT8, 78% for AT180, and 25% for pY18 (Figures 4C and 4E). Thus, Fyn knockout not only protects from the accumulation of hyperphosphorylated tau but also halts the transition of tau from a soluble to an insoluble state.

Synaptic Accumulation of Tau Is Decreased in Tg/Fyn$^{-/-}$ Mice

The localization of hyperphosphorylated tau to the synaptic compartment is an early event in AD pathogenesis in both human patients and tau transgenic mice (Yoshiyama et al., 2007). Tau is critical to the dendritic and nanoscale organization of Fyn, and suppression of the tau-Fyn interaction blocks the induction of an Aβ-induced, NMDAR-mediated postsynaptic excitotoxic cascade (Ittner et al., 2010; Padmanabhan et al., 2019). It has also been reported that Fyn itself regulates the dendritic distribution of tau through its activation by Aβ and the prion protein PrP^{c} (Larson et al., 2012), which when viewed together with the finding that Fyn is crucial in regulating the dendritic translation of tau (Li and Götz, 2017) illustrates that the roles of tau and Fyn in synaptic targeting are potentially reciprocal in nature. Following our histological observations of downregulated phospho-tau in dendrites (Figures 2 and 3) and immunoblots demonstrating a global loss of hyperphosphorylated tau (Figure 4), we next sought to directly assess the levels of dendritic tau in the Tg/Fyn$^{-/-}$ model through synaptosomal fractionation (Figure 5). The final synaptosome-enriched pellet of the fractionation procedure was serially fractionated as for whole-brain lysates above, thereby providing a synaptosomal RAB fraction containing soluble synaptic proteins and a synaptosomal RIPA/SDS fraction that comprised insoluble and membrane-associated proteins (Figure 5A). These preparations were then analyzed by immunoblot.

Total and phospho-tau levels were dramatically reduced in both RAB- and RIPA/SDS-synaptosomes. Unlike in the whole-brain RAB-soluble fraction, total tau and pY18-tau levels were significantly decreased by 29% and 27%, respectively (Figures 5B and 5D). Furthermore, the differences between rTg4510 and Tg/Fyn$^{-/-}$ AT8 and AT180 phospho-tau in the RAB-soluble synaptosomal fraction were greater than at the whole-brain level (for AT8, 62% versus 33% reduction; for AT180, 60% versus 42% reduction, comparing rTg4510 synaptosomes versus whole-brain lysates, respectively), an observation in line with previous reports that highlight an enhancement of dendritic targeting upon pseudophosphorylation at these sites (Hoover et al., 2010; Xia et al., 2015). Interestingly, depletions of all forms of RIPA/SDS-soluble tau in the synaptosomes of Tg/Fyn$^{-/-}$ mice

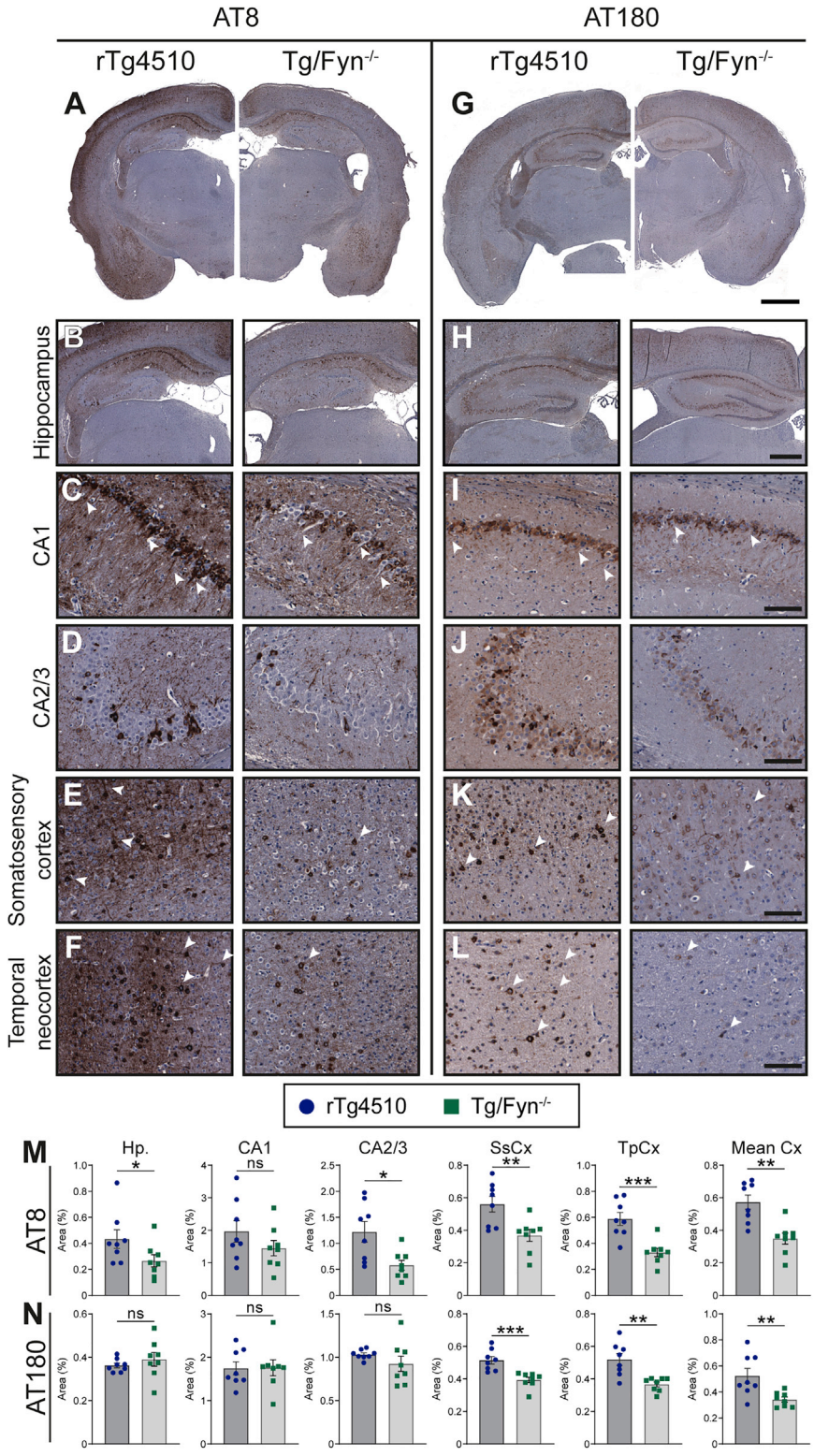

Figure 3. Tg/Fyn$^{-/-}$ Mice Exhibit a Region- and Epitope-Specific Decrease in Hyperphosphorylated Tau

(A–L) Representative images of rTg4510 and Tg/Fyn$^{-/-}$ mouse strains immunostained for tau phosphoepitopes AT8 and AT180. Arrowheads signify the accumulation of phospho-tau in the apical dendrites that are largely absent in Tg/Fyn$^{-/-}$ mice, within the CA1 region (C and I) or neocortical regions (E, F, K, and L). Scale bars represent 1,000 μm (A and G), 500 μm (B and H), and 100 μm (C–F and I–L).

(M and N) Quantification of thresholded DAB immunolabeling presented as the percentage area of the given region for AT8 and AT180, respectively. Data are presented as mean ± SEM; n = 8 mice. *p < 0.05; **p < 0.01; ***p < 0.001; and ns, not significant (t test).

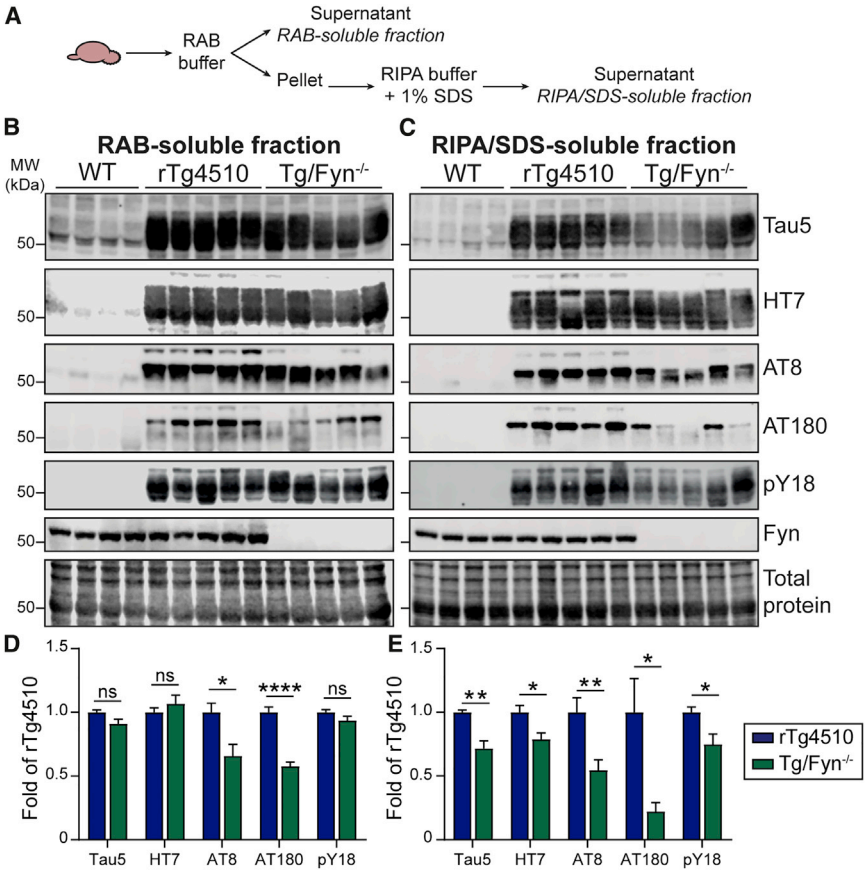

Figure 4. Tau Solubility and Phosphorylation Are Altered in Tg/Fyn$^{-/-}$ Mice

(A) Schematic depicting serial fractionation protocol used in the analysis of tau solubility in whole-brain lysates.

(B and C) RAB- and RIPA/SDS-fractionated lysates probed by immunoblot for total mouse and human tau (Tau5), total human tau (HT7), pathological tau species AT8 and AT180, pY18 tau, and Fyn (not quantified). Blots were normalized by total protein staining.

(D and E) Quantification of (B) and (C), presented as fold change relative to rTg4510 levels. Data are presented as mean ± SEM; n = 4, 5, and 5 for WT, rTg4510, and Tg/Fyn$^{-/-}$ mice, respectively. *p < 0.05; **p < 0.01; ****p < 0.0001; and ns, not significant (one-way ANOVA with Holm-Sidak's multiple comparisons test).

did not exceed those observed at the whole-brain level, suggesting that this more fibrillar form of tau is less mobile (Figures 5C and 5E).

Importantly, the loss of synaptic tau targeting in Tg/Fyn$^{-/-}$ was not due to a disruption of the Fyn/ERK/S6 translational activation pathway (Li and Götz, 2017; Roux et al., 2007) as assessed by ERK1/2 phosphorylation (Figure S4), thereby underscoring the dependence of this pathway on Aβ. Taken together, these results support the notion that Fyn plays an important role in the synaptic accumulation of pathological tau.

Tg/Fyn$^{-/-}$ Tau Seeds Exhibit Reduced Efficiency in Inducing Tau Aggregation and Generate Less-Ordered Aggregate Morphologies in Tau Biosensor Cells

The fact that tau pathology spreads throughout the human brain in a transneuronal, region-to-region manner is thought to reflect a prion-like ability of the tau protein to seed its own aggregation (Clavaguera et al., 2013; de Calignon et al., 2012; Polanco et al., 2018b). Proteopathic tau seeding is among the earliest markers of tauopathy *in vivo*, preceding histopathological staining for phospho-tau epitopes (Holmes et al., 2014), and occurs in a time- and concentration-threshold-dependent manner (Polanco et al., 2016). Hyperphosphorylated high-molecular-weight tau species are the most efficient inducers of tau aggregation, suggesting a role in the transcellular propagation of tauopathy (Takeda et al., 2015). As Tg/Fyn$^{-/-}$ mice display diminished formation of NFTs and hyperphosphorylated tau (Figures 1, 2, and 3), together with decreased insoluble total and phosphorylated tau levels (Figure 4), we investigated whether Tg/Fyn$^{-/-}$ tau seeds were impaired in their ability to elicit aggregation in fluorescence resonance energy transfer (FRET) tau biosensor cells. These cells are an engineered line of HEK293T cells that stably co-expresses the tau microtubule-binding repeat domain (RD) with the pathological FTLD P301S mutation conjugated to CFP and YFP proteins (RD-CFP and RD-YFP tau moieties), the aggregation of which following treatment with exogenous tau seeds generates a FRET signal that is quantifiable by flow cytometry and fluorescence microscopy (Holmes et al., 2014).

Brain lysates were produced from WT, rTg4510, and Tg/Fyn$^{-/-}$ brains and used to treat HEK293T biosensor cells for 72 h (Figure 6). Remarkably, Tg/Fyn$^{-/-}$-treated biosensor cells displayed a nearly 4-fold decrease in FRET positivity compared to cells seeded with rTg4510 lysates (1.32% versus 0.37% of cells were FRET-positive; Figures 6C and 6D), corresponding to a significant 73% decrease in FRET signal integrated density (Figure 6I). When analyzed microscopically, the reduction in FRET signal was reflected by a decrease of an even greater magnitude in the percentage area of aggregates, with Tg/Fyn$^{-/-}$-treated cells displaying levels of only 12% of those in rTg4510-treated cells.

In order to understand why the magnitude of this reduction was greater than when cells were assessed by FRET, we sought to establish if the size and morphology of the cytoplasmic tau aggregates induced by Tg/Fyn$^{-/-}$ lysates were different to those in rTg4510-treated cells. To this end, inclusion morphology was semiquantitatively assessed according to a system similar to that used by Sanders et al. (2014), who originally graded the morphology of tau aggregates within biosensor cells seeded with tau derived from different human tauopathy samples to delineate prion-like strains of tau aggregate conformers

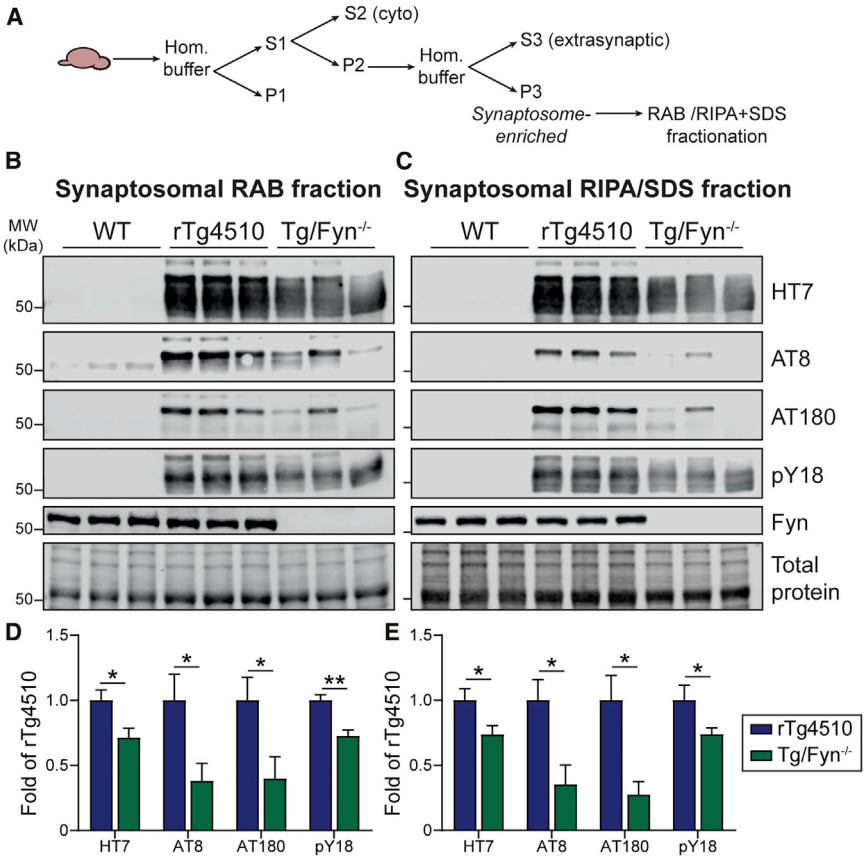

Figure 5. Total and Phospho-Tau Levels Are Reduced in Tg/Fyn$^{-/-}$ Synaptosomes

(A) Overview of protocol for the generation of crude synaptosomal RAB- and RIPA/SDS-soluble tau fractions.

(B and C) RAB-soluble (B) and RIPA/SDS-soluble (C) synaptosomes were probed for HT7, AT8, AT180, pY18, and Fyn. Immunoblots were normalized by total protein staining.

(D and E) Quantification of (B) and (C), respectively, represented as fold change of rTg4510 levels. Data are presented as mean ± SEM; n = 3 mice. *p < 0.05 and **p < 0.01 (one-way ANOVA with Holm-Sidak's multiple comparisons test).

(Figure 6K). Our results revealed that tau inclusions in Tg/Fyn$^{-/-}$-treated cells were indeed morphologically shifted to a more punctate or fragmented phenotype, in stark contrast to the largely ordered formations observed in their rTg4510-treated counterparts (Figure 6L). Thus, Tg/Fyn$^{-/-}$ tau seeds are limited in their ability to induce aggregation *in vitro* and are perhaps less able to self-assemble into higher-order, more complex structures.

Pseudophosphorylation of Residue Y18 Enhances Tau Fibrillization *In Vitro*

Finally, we aimed to clarify whether phosphorylation of pY18 was sufficient to affect tau fibrillization (Figure 7), in contrast to a more generic physical tau-Fyn interaction. To investigate this, we produced full-length recombinant human tau (hTau) bearing either the phospho-mimetic point mutation Y18E or the non-polar mutation Y18A. Fibrillization was induced *in vitro* with heparin (Goedert et al., 1996) and monitored with Thioflavin T (ThioT) fluorescence for 72 h (Figure 7A). Interestingly, Y18E-tau displayed increased fibrillization relative to nonmutant hTau, reaching maximal ThioT fluorescence levels of ~130% after 72-h incubation. In contrast, the fibrillization of Y18A-tau was strongly inhibited. Kinetic modeling revealed Y18E-tau accumulated a significantly larger area under the curve (Figure 7B), although interestingly, the half-time of maximum aggregation ($t_{1/2}$) and lag time (t_{lag}) for each of the types of tau were comparable (~40–45 h and ~25–32 h, respectively), suggesting similar rates of aggregation (Figure 7A). Therefore, Y18E appears to stabilize and trap tau in a higher-molecular-weight state while not directly catalyzing its aggregation. In concordance with this notion, TOC1 dot-blot demonstrated increased Y18E-tau oligomers after heparin-induced aggregation (Figures 7C and 7D). Thus, Fyn appears to act as a direct regulator of tau aggregation, a mechanism enhanced by its phosphorylation of Y18.

DISCUSSION

Fyn is the major intermediary in the pathological signaling cascade of Aβ to tau (Ittner et al., 2010; Li and Götz, 2017). In the current study, we sought to determine whether Fyn also drives tauopathy in the absence of Aβ. To address this question, we generated a novel Tg/Fyn$^{-/-}$ mouse strain and complemented the *in vivo* analyses with *in vitro* studies and incubations of tau biosensor cells. Together, our work indicates that Fyn is a key regulator of tau pathology.

The accumulation of tau as insoluble NFTs is a hallmark of AD and correlates with impaired cognition (Nelson et al., 2012). Intriguingly and unexpectedly, Gallyas silver staining for mature NFTs in Tg/Fyn$^{-/-}$ mice revealed a 94% decrease in overall cortical NFT burden relative to that in rTg4510 mice. The magnitude of this decrease was greater than that observed for TOC1-tau oligomers, pY18, AT8, or AT180 cortical immunolabeling or total and phospho-tau markers in the RIPA/SDS-soluble tau fraction. This suggests different thresholds for different phosphoepitopes and tau oligomers, tau species, and assemblies that would be on a path to develop fibrils in a nonmutant mouse. However, in Tg/Fyn$^{-/-}$ mice, there is a pronounced and selective decrease in the formation of fibrillar, insoluble high-molecular-weight tau. This had not previously been explored, given our limited understanding of the function of Fyn, which mostly prescribes a role of Aβ in pathways relating to tau-dependent excitotoxicity in the postsynapse (reviewed by Nygaard, 2018). Interestingly, and possibly related to Fyn's predominantly synaptic localization (Ohnishi et al., 2011) or the strong reduction in phospho- and total tau in whole-brain fractions, we observed

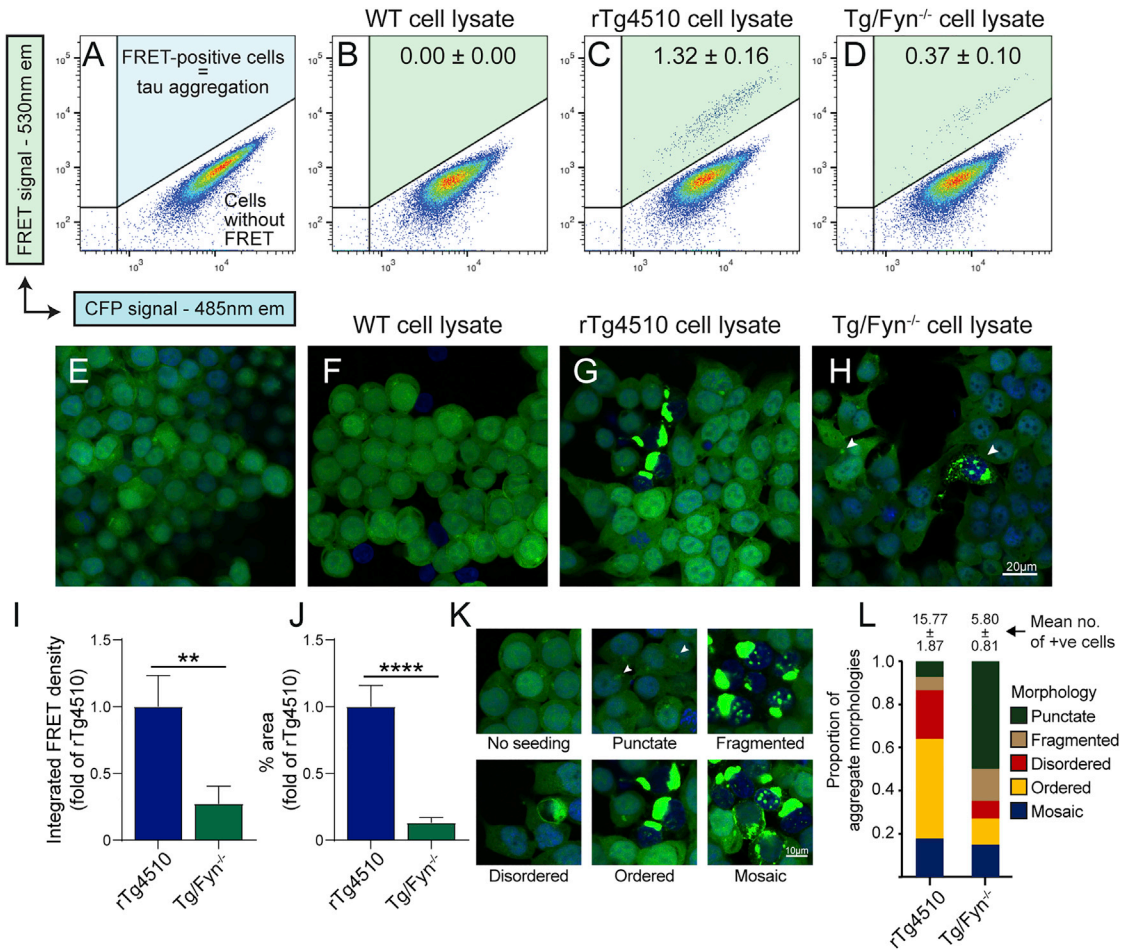

Figure 6. Tg/Fyn$^{-/-}$ Brain Lysates Induce Less Tau Seeding and More Fragmented Inclusions in FRET Tau Biosensor Cells

(A–D) FRET tau biosensor cells were treated with PBS brain lysates for 72 h, whereupon they were analyzed by FRET flow cytometry and confocal microscopy. Representative FRET flow cytometry plots with average percentage of FRET-positive cells (mean ± SEM, n = 3 mice per experiment, 40,000 cells analyzed per experiment). No aggregates were observed for untreated control (A) or WT lysates (B).

(E–H) Representative 20× confocal fluorescence images of biosensor cells after treatment with PBS alone (E) or brain lysates (F–H), with FRET-positive tau aggregates shown in bright green and nuclear Hoechst staining in blue. Arrowhead in (H) denotes punctate aggregate. Scale bar, 10 μm.

(I) Quantification of (C) and (D). The integrated FRET signal, the product of the mean FRET fluorescence intensity and the percentage of FRET-positive cells, was calculated and data normalized to rTg4510 FRET signals. Data are presented as mean ± SEM; n = 3 mice per experiment, 40,000 cells per experiment analyzed from two replicate experiments. **$p < 0.01$ (t test).

(J) Confocal images were thresholded by intensity, and the percentage area of tau aggregates, normalized to DAPI area, was calculated. Data are presented as mean ± SEM and expressed as a fold change of rTg4510. n = 3 mice per experiment, with at least four images per experiment. ****$p < 0.0001$ (t test).

(K) To semiquantitatively assess the morphology of biosensor cells seeded with transgenic mouse PBS lysates, a variety of aggregate phenotypes (Sanders et al., 2014) were delineated: no seeding, punctate (arrowhead), fragmented, disordered, ordered, and mosaic. Scale bar, 5 μm.

(L) Inclusion-positive rTg4510 and Tg/Fyn$^{-/-}$-seeded cells were manually examined, and the relative proportion of each morphology defined in (K) was quantified. The mean number of positive cells for each genotype ± SEM is displayed (n = 3).

impaired targeting of tau to the synaptic domain in the Tg/Fyn$^{-/-}$ mice.

There are several scenarios whereby Fyn could regulate NFT biogenesis *in vivo*. The most obvious, and most readily supported by our histological and biochemical data (Figures 2, 3, and 4), relates to the apparent Fyn-dependent reduction in tau hyperphosphorylation at serine and threonine residues in the proline-rich region of tau. Furthermore, NFT formation could be enhanced by the apparent role of Fyn in an increased somatic subcellular localization of pY18 tau (Figures 2C and 2H). Physiological tau function is governed by phosphorylation, yet in a disease setting, excessive phosphorylation drives the release of the protein from microtubules and its fibrillization (Alonso et al., 2001; Despres et al., 2017). Fyn acts widely in neuronal and non-neuronal cells as an integrator of signaling cascades and activates numerous serine/threonine kinases through tyrosine phosphorylation (Martin et al., 2013; Salmond et al., 2009). Biochemical analyses of whole-brain tau solubility highlighted a preferential loss of AT8 and AT180 in the soluble tau fraction preceding reduced accumulation of total and pY18-tau in the

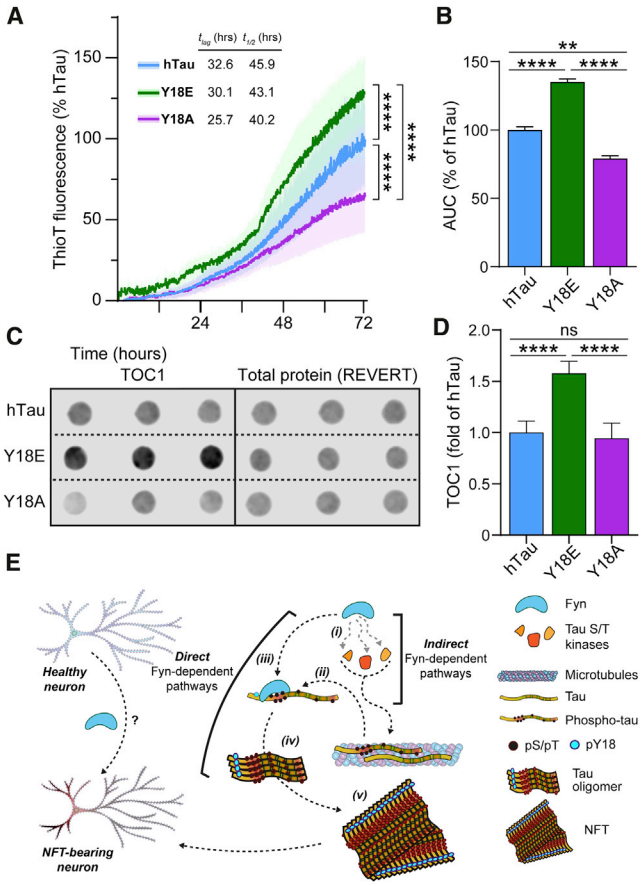

Figure 7. Enhanced *In Vitro* Tau Fibrillization with Y18 Pseudophosphorylation Reveals a Unifying Role for Fyn in Tauopathies that Lack Aβ

(A) Fibrillization of recombinant full-length human tau (hTau) and hTau harboring Y18 phospho-mimetic (Y18E) or non-polar (Y18A) point mutations was induced by heparin and monitored by thioflavin T (ThioT) fluorescence over a 72-h period. Curves represent mean ± SEM (as shaded envelope) and are an average from n = 3 experiments, each performed in triplicate. Kinetic constants $t_{1/2}$ and t_{lag} (time of half-maximum aggregation and lag time, respectively) were derived from curve fitting to a sigmoid function. ****p < 0.0001 (two-way ANOVA for main effect in time versus hTau species, with Tukey's multiple comparisons test).

(B) Area under the curve (AUC) for each curve in (A), normalized to hTau. Data represent mean ± SEM; n = 3 replicates (in triplicate). **p < 0.01 and ****p < 0.0001 (one-way ANOVA with Holm-Sidak's multiple comparisons test).

(C) Dot blot for TOC1 of completed 72-h tau aggregation reaction. Presented dot blots were from a separate experiment and were probed in triplicate.

(D) Quantification of (C). Data represent mean ± SEM; n = 3 replicates. ****p < 0.0001; and ns, not significant (one-way ANOVA with Holm-Sidak's multiple comparisons test).

(E) A model for Fyn's regulatory role in NFT biogenesis in non-Aβ tauopathies. Fyn activates prominent tau serine/threonine kinases (i) and thereby indirectly enhances the hyperphosphorylation of tau and its resultant release from microtubules (ii). Hyperphosphorylated or "free" tau not bound to microtubules is then phosphorylated by Fyn at Y18 (iii), thereby directly increasing the oligomerization of tau (iv) and its deposition as NFTs (v). Processes supported by our data or within the literature are indicated by black arrows, whereas hypothetical mechanisms are indicated by gray arrows.

insoluble tau fraction, suggesting that Fyn may be upstream of the hyperphosphorylation events that trigger aggregation (Figure 4). This report is not the first to observe decreased serine/threonine phosphorylation of tau with genetic (Minami et al., 2012) or pharmacological Fyn depletion (Kaufman et al., 2015), although these studies were performed using animal models overexpressing mutant amyloid precursor protein (APP) and thereby displaying Aβ pathology. Perhaps more cogently, increased tau serine/threonine phosphorylation was observed in a mouse model expressing constitutively active Fyn (Xia and Götz, 2014).

Prominent tau kinases that may be activated by Fyn-mediated tyrosine phosphorylation include GSK-3β (Lesort et al., 1999), Cdk5 (Sasaki et al., 2002) and the mitogen-activated protein kinase (MAPK) p38 (Kapus et al., 1999), although the degree to which each of these kinases is activated in our model was not tested. It is noteworthy that the activity of the MAPK ERK1/2, which not only phosphorylates tau directly at many serine/threonine sites but also mediates local tau synthesis after Aβ treatment, was unchanged among WT, rTg4510, and Tg/Fyn$^{-/-}$ mice (Li and Götz, 2017), highlighting the *in vivo* requirement of a stimulus, such as (but not limited to) Aβ, to induce this cascade.

Importantly, our data also highlight an underappreciated role for Fyn's phosphorylation of tau at Y18 in tau aggregation, oligomerization, and NFT formation. We found that pseudophosphorylated Y18E mutant tau displayed significantly enhanced fibrillization, whereas Y18A-tau exhibited strongly curtailed aggregation. This could be interpreted as suggesting that tau aggregation is driven by the local charge of the N-terminus, with the phosphorylation of tau at Y18 inducing a conformational change that stabilizes high-molecular-weight conformers of tau and, ultimately, promotes the formation of NFTs. Further (albeit circumstantial) evidence for a role for pY18 in NFT formation comes from nanostructural reconstruction of the PHF-tau core with cryo-electron microscopy, which has revealed a role for N-terminal residues 7–9 of tau in stabilizing the protofilament interface of both paired-helical and straight filaments, a site in close proximity to Y18 but hundreds of residues away from the amyloidogenic core (Fitzpatrick et al., 2017; Stöhr et al., 2017). Given our findings that pY18-tau and total tau levels correlate strongly in RAB- and RIPA/SDS-soluble fractions, it is tempting to hypothesize that Y18 tau phosphorylation is a rate-limiting step in NFT biogenesis. More specifically, the fact that pY18 staining was not reduced as completely as NFT burden suggests that the amelioration of the NFT burden in Tg/Fyn$^{-/-}$ mice occurs through the restriction of the phosphorylation of this epitope below a required threshold.

Another, possibly related mechanism through which Fyn may mediate NFT formation relates to the propensity of these molecules to undergo phase transitions from the soluble to the insoluble state. Proteins with intrinsically disordered regions (such as the long N-terminal projection domain of tau and the unique SH4 domain of Fyn) and modular binding motifs (such as tau's four microtubule-binding repeats and Fyn's SH3 domain) (Li et al., 2012) drive liquid-liquid phase separation, a biophysical phenomenon through which a molecule will demix from the surrounding cellular milieu and become enriched in highly dynamic membraneless organelles (reviewed by Shin and Brangwynne,

2017). Aberrant phase behavior, subsequent gelation, and eventual amyloidogenic aggregation is increasingly viewed as a generalized mechanism that drives neurodegenerative disorders (Narayanan et al., 2019), as postulated for proteins FUS (Patel et al., 2015), hnRNPA1 (Molliex et al., 2015), and TIA1 (Mackenzie et al., 2017) in amyotrophic lateral sclerosis, and for TDP-43 in FTLD (Mann et al., 2019).

Tau phase separation, a phenomenon observed *in vitro* and largely mediated by its microtubule-binding repeats, can nucleate, and is gated by, microtubules (Ambadipudi et al., 2017; Hernández-Vega et al., 2017; Tan et al., 2019). Furthermore, the ability of tau to reversibly demix is enhanced by RNA binding and phosphorylation and prolonged maintenance of tau in the condensed phase leads to the formation of amyloid-like fibrils (Wegmann et al., 2018; Zhang et al., 2017). Interestingly, the SH3 domain of Fyn also undergoes phase separation upon binding with the RNA-binding protein hnRNPA2 (Amaya et al., 2018). Moreover, considering that protein charge distribution (Nott et al., 2015) and tyrosine content (Wang et al., 2018) regulate phase separation, we speculate that pY18-tau may display altered phase behavior. In agreement with this, chemical inhibition of Fyn in neuronal cultures has been shown to block not only tau hyperphosphorylation but also its accumulation in stress granules (Vanderweyde et al., 2016), which are phase-separated membraneless organelles that are thought to represent nucleation "hot-spots" in tauopathy through the pathological association of tau with the RNA-binding protein TIA1 (Apicco et al., 2018; Maziuk et al., 2018). Whether physiological or pathological tau-Fyn binding or pY18 phosphorylation specifically promotes the phase separation of tau and Fyn and the subsequent fibrillization of the former remains to be established.

Given that disease-related serine/threonine phosphorylation of tau increases Fyn's affinity for tau and that tau's binding to Fyn-SH3 regulates phosphorylation at Y18 (Bhaskar et al., 2010; Bhaskar et al., 2005), we propose that the role of Fyn in enhancing tau aggregation may occur through both indirect and direct pathways (see Figure 7E). Fyn may first gate the activity of important tau kinases, thereby indirectly promoting the release of tau from microtubules; this could then result in increased tau-Fyn binding, which may boost Y18 phosphorylation and/or induce phase separation, leading to eventual fibrillization of tau into NFTs. What regulates the activity of Fyn in non-AD tauopathies, however, remains obscure.

The interneuronal propagation and prion-like seeding of tau *in vivo* is well characterized (de Calignon et al., 2012; Polanco et al., 2018b; Wu et al., 2016; Yamada et al., 2014), and the conformational shift of tau that promotes templated proteopathic aggregation is among the earliest detectable pathological alterations (Holmes et al., 2014). Hyperphosphorylated, high-molecular-weight tau is most efficient at transducing recipient cells (Takeda et al., 2015), although many forms of tau (including disaggregated monomers) are capable of inducing *de novo* tau seeding (Mirbaha et al., 2018). Our studies in tau biosensor cells revealed that Tg/Fyn$^{-/-}$ brains contain tau conformers that induce less tau aggregation and that these aggregates manifest as smaller, more fragmented entities. This lends further support to our findings that tau fibrillization is blocked in the absence of Fyn *in vivo* or that Fyn knockout may contribute to tau forming an alternative prionoid strain (Sanders et al., 2014).

To conclude, our study identifies a role for Fyn as a key regulator of pathological tau aggregation separate from its previously established role in transducing Aβ signaling in AD. Further experiments are required to dissect exactly which pathways are altered in the absence of Fyn, although the phosphorylation of tau at Y18 appears to significantly influence tau fibril formation. Targeting Fyn in order to block not only Aβ-induced neurotoxicity but also tau oligomerization and fibrillization may represent a therapeutic strategy not only for AD but also for other tauopathies.

STAR★METHODS

Detailed methods are provided in the online version of this paper and include the following:

- KEY RESOURCES TABLE
- RESOURCE AVAILABILITY
  - Lead contact
  - Materials availability
  - Data and Code Availability
- EXPERIMENTAL MODEL AND SUBJECT DETAILS
  - Animals
  - Cell culture
- METHOD DETAILS
  - Behavioral analyses and brain mass measurements
  - Immunohistochemistry and immunofluorescence
  - Whole-brain RAB-RIPA/SDS fractionation
  - Synaptosomal fractionation
  - PBS brain lysates
  - Immunoblot and dot-blot
  - Aggregation assays with tau biosensor cells
  - FRET flow cytometry
  - Microscopy of cells grown on coverslips
  - Molecular cloning
  - Recombinant tau expression
  - Thioflavin T tau fibrillization assay
  - Image and immunoblot analysis
- QUANTIFICATION AND STATISTICAL ANALYSIS

SUPPLEMENTAL INFORMATION

Supplemental Information can be found online at https://doi.org/10.1016/j.celrep.2020.108045.

ACKNOWLEDGMENTS

We thank Tishila Palliyaguru for general laboratory coordination; Linda Cumner and QBI Animal Facility staff for animal maintenance; Chuanzhou Li for assisting in project conception, direction, and critical reading; Joey Benetatos for stimulating and valuable discussion; Pranesh Padmanabhan for advice with ThioT curve fitting; and Dr. Liz Cooper-Williams for assistance writing image analysis scripts. Imaging/analysis was performed at the Queensland Brain Institute's Advanced Microscopy Facility using Zeiss LSM710 and fluorescence/brightfield slide scanner microscopes (generously supported by the Australian Government through Australian Research Council (ARC) Linkage Infrastructure, Equipment and Facilities (LIEF) grants LE130100078 and LE100100074). We also thank Dr. Nicholas Kanaan for generously providing

TOC1 antibody. This research was supported by the Estate of Dr. Clem Jones AO, the State Government of Queensland, the Federal Government of Australia (ACT900116), and grants from the Australian Research Council (ARC DP190102789) and the National Health and Medical Research Council (NHMRC) (GNT1161133).

AUTHOR CONTRIBUTIONS

A.B., J.C.P., and J.G. designed and interpreted the experiments; A.B. performed the experiments and analyzed the data; and A.B. wrote the manuscript, which was edited by J.G. and J.C.P.

DECLARATION OF INTERESTS

The authors declare no competing interests.

Received: October 24, 2019
Revised: June 14, 2020
Accepted: July 27, 2020
Published: August 18, 2020

REFERENCES

Alonso, A., Zaidi, T., Novak, M., Grundke-Iqbal, I., and Iqbal, K. (2001). Hyperphosphorylation induces self-assembly of tau into tangles of paired helical filaments/straight filaments. Proc. Natl. Acad. Sci. USA *98*, 6923–6928.

Amaya, J., Ryan, V.H., and Fawzi, N.L. (2018). The SH3 domain of Fyn kinase interacts with and induces liquid-liquid phase separation of the low-complexity domain of hnRNPA2. J. Biol. Chem. *293*, 19522–19531.

Ambadipudi, S., Biernat, J., Riedel, D., Mandelkow, E., and Zweckstetter, M. (2017). Liquid-liquid phase separation of the microtubule-binding repeats of the Alzheimer-related protein Tau. Nat. Commun. *8*, 275.

Apicco, D.J., Ash, P.E.A., Maziuk, B., LeBlang, C., Medalla, M., Al Abdullatif, A., Ferragud, A., Botelho, E., Ballance, H.I., Dhawan, U., et al. (2018). Reducing the RNA binding protein TIA1 protects against tau-mediated neurodegeneration in vivo. Nat. Neurosci. *21*, 72–80.

Asai, H., Ikezu, S., Tsunoda, S., Medalla, M., Luebke, J., Haydar, T., Wolozin, B., Butovsky, O., Kügler, S., and Ikezu, T. (2015). Depletion of microglia and inhibition of exosome synthesis halt tau propagation. Nat. Neurosci. *18*, 1584–1593.

Baker, S., Polanco, J.C., and Götz, J. (2016). Extracellular vesicles containing P301L mutant tau accelerate pathological tau phosphorylation and oligomer formation but do not seed mature neurofibrillary tangles in ALZ17 mice. J. Alzheimers Dis. *54*, 1207–1217.

Belzung, C., and Griebel, G. (2001). Measuring normal and pathological anxiety-like behaviour in mice: a review. Behav. Brain Res. *125*, 141–149.

Bhaskar, K., Yen, S.H., and Lee, G. (2005). Disease-related modifications in tau affect the interaction between Fyn and Tau. J. Biol. Chem. *280*, 35119–35125.

Bhaskar, K., Hobbs, G.A., Yen, S.H., and Lee, G. (2010). Tyrosine phosphorylation of tau accompanies disease progression in transgenic mouse models of tauopathy. Neuropathol. Appl. Neurobiol. *36*, 462–477.

Biernat, J., Gustke, N., Drewes, G., Mandelkow, E.M., and Mandelkow, E. (1993). Phosphorylation of Ser262 strongly reduces binding of tau to microtubules: distinction between PHF-like immunoreactivity and microtubule binding. Neuron *11*, 153–163.

Braak, H., Alafuzoff, I., Arzberger, T., Kretzschmar, H., and Del Tredici, K. (2006). Staging of Alzheimer disease-associated neurofibrillary pathology using paraffin sections and immunocytochemistry. Acta Neuropathol. *112*, 389–404.

Busche, M.A., Wegmann, S., Dujardin, S., Commins, C., Schiantarelli, J., Klickstein, N., Kamath, T.V., Carlson, G.A., Nelken, I., and Hyman, B.T. (2019). Tau impairs neural circuits, dominating amyloid-β effects, in Alzheimer models in vivo. Nat. Neurosci. *22*, 57–64.

Chin, J., Palop, J.J., Yu, G.-Q., Kojima, N., Masliah, E., and Mucke, L. (2004). Fyn kinase modulates synaptotoxicity, but not aberrant sprouting, in human amyloid precursor protein transgenic mice. J. Neurosci. *24*, 4692–4697.

Chin, J., Palop, J.J., Puoliväli, J., Massaro, C., Bien-Ly, N., Gerstein, H., Scearce-Levie, K., Masliah, E., and Mucke, L. (2005). Fyn kinase induces synaptic and cognitive impairments in a transgenic mouse model of Alzheimer's disease. J. Neurosci. *25*, 9694–9703.

Clavaguera, F., Akatsu, H., Fraser, G., Crowther, R.A., Frank, S., Hench, J., Probst, A., Winkler, D.T., Reichwald, J., Staufenbiel, M., et al. (2013). Brain homogenates from human tauopathies induce tau inclusions in mouse brain. Proc. Natl. Acad. Sci. USA *110*, 9535–9540.

D'Amelio, M., Cavallucci, V., Middei, S., Marchetti, C., Pacioni, S., Ferri, A., Diamantini, A., De Zio, D., Carrara, P., Battistini, L., et al. (2011). Caspase-3 triggers early synaptic dysfunction in a mouse model of Alzheimer's disease. Nat. Neurosci. *14*, 69–76.

de Calignon, A., Polydoro, M., Suárez-Calvet, M., William, C., Adamowicz, D.H., Kopeikina, K.J., Pitstick, R., Sahara, N., Ashe, K.H., Carlson, G.A., et al. (2012). Propagation of tau pathology in a model of early Alzheimer's disease. Neuron *73*, 685–697.

Despres, C., Byrne, C., Qi, H., Cantrelle, F.-X., Huvent, I., Chambraud, B., Baulieu, E.-E., Jacquot, Y., Landrieu, I., Lippens, G., and Smet-Nocca, C. (2017). Identification of the Tau phosphorylation pattern that drives its aggregation. Proc. Natl. Acad. Sci. USA *114*, 9080–9085.

Fá, M., Puzzo, D., Piacentini, R., Staniszewski, A., Zhang, H., Baltrons, M.A., Li Puma, D.D., Chatterjee, I., Li, J., Saeed, F., et al. (2016). Extracellular tau oligomers produce an immediate impairment of LTP and memory. Sci. Rep. *6*, 19393.

Fitzpatrick, A.W.P., Falcon, B., He, S., Murzin, A.G., Murshudov, G., Garringer, H.J., Crowther, R.A., Ghetti, B., Goedert, M., and Scheres, S.H.W. (2017). Cryo-EM structures of tau filaments from Alzheimer's disease. Nature *547*, 185–190.

Forrest, S.L., Kril, J.J., Stevens, C.H., Kwok, J.B., Hallupp, M., Kim, W.S., Huang, Y., McGinley, C.V., Werka, H., Kiernan, M.C., et al. (2018). Retiring the term FTDP-17 as MAPT mutations are genetic forms of sporadic frontotemporal tauopathies. Brain *141*, 521–534.

Frandemiche, M.L., De Seranno, S., Rush, T., Borel, E., Elie, A., Arnal, I., Lanté, F., and Buisson, A. (2014). Activity-dependent tau protein translocation to excitatory synapse is disrupted by exposure to amyloid-beta oligomers. J. Neurosci. *34*, 6084–6097.

Gamache, J., Benzow, K., Forster, C., Kemper, L., Hlynialuk, C., Furrow, E., Ashe, K.H., and Koob, M.D. (2019). Factors other than hTau overexpression that contribute to tauopathy-like phenotype in rTg4510 mice. Nat. Commun. *10*, 2479.

Gasteiger, E., Hoogland, C., Gattiker, A., Duvaud, S., Wilkins, M.R., Appel, R.D., and Bairoch, A. (2005). Protein identification and analysis tools on the ExPASy server. In The Proteomics Protocols Handbook, J.M. Walker, ed. (Humana Press), pp. 571–607.

Goedert, M., Jakes, R., Spillantini, M.G., Hasegawa, M., Smith, M.J., and Crowther, R.A. (1996). Assembly of microtubule-associated protein tau into Alzheimer-like filaments induced by sulphated glycosaminoglycans. Nature *383*, 550–553.

Goodwin, L.O., Splinter, E., Davis, T.L., Urban, R., He, H., Braun, R.E., Chesler, E.J., Kumar, V., van Min, M., Ndukum, J., et al. (2019). Large-scale discovery of mouse transgenic integration sites reveals frequent structural variation and insertional mutagenesis. Genome Res. *29*, 494–505.

Goto, J., Tezuka, T., Nakazawa, T., Sagara, H., and Yamamoto, T. (2008). Loss of Fyn tyrosine kinase on the C57BL/6 genetic background causes hydrocephalus with defects in oligodendrocyte development. Mol. Cell. Neurosci. *38*, 203–212.

Götz, J., Chen, F., van Dorpe, J., and Nitsch, R.M. (2001). Formation of neurofibrillary tangles in P301l tau transgenic mice induced by Abeta 42 fibrils. Science *293*, 1491–1495.

Grant, S.G., O'Dell, T.J., Karl, K.A., Stein, P.L., Soriano, P., and Kandel, E.R. (1992). Impaired long-term potentiation, spatial learning, and hippocampal development in fyn mutant mice. Science *258*, 1903–1910.

Grundke-Iqbal, I., Iqbal, K., Tung, Y.C., Quinlan, M., Wisniewski, H.M., and Binder, L.I. (1986). Abnormal phosphorylation of the microtubule-associated protein tau (tau) in Alzheimer cytoskeletal pathology. Proc. Natl. Acad. Sci. USA *83*, 4913–4917.

Hernández-Vega, A., Braun, M., Scharrel, L., Jahnel, M., Wegmann, S., Hyman, B.T., Alberti, S., Diez, S., and Hyman, A.A. (2017). Local nucleation of microtubule bundles through tubulin concentration into a condensed tau phase. Cell Rep. *20*, 2304–2312.

Ho, G.J., Hashimoto, M., Adame, A., Izu, M., Alford, M.F., Thal, L.J., Hansen, L.A., and Masliah, E. (2005). Altered p59Fyn kinase expression accompanies disease progression in Alzheimer's disease: implications for its functional role. Neurobiol. Aging *26*, 625–635.

Holmes, B.B., Furman, J.L., Mahan, T.E., Yamasaki, T.R., Mirbaha, H., Eades, W.C., Belaygorod, L., Cairns, N.J., Holtzman, D.M., and Diamond, M.I. (2014). Proteopathic tau seeding predicts tauopathy in vivo. Proc. Natl. Acad. Sci. USA *111*, E4376–E4385.

Hoover, B.R., Reed, M.N., Su, J., Penrod, R.D., Kotilinek, L.A., Grant, M.K., Pitstick, R., Carlson, G.A., Lanier, L.M., Yuan, L.L., et al. (2010). Tau mislocalization to dendritic spines mediates synaptic dysfunction independently of neurodegeneration. Neuron *68*, 1067–1081.

Hutton, M., Lendon, C.L., Rizzu, P., Baker, M., Froelich, S., Houlden, H., Pickering-Brown, S., Chakraverty, S., Isaacs, A., Grover, A., et al. (1998). Association of missense and 5′-splice-site mutations in tau with the inherited dementia FTDP-17. Nature *393*, 702–705.

Ittner, L.M., Ke, Y.D., Delerue, F., Bi, M., Gladbach, A., van Eersel, J., Wölfing, H., Chieng, B.C., Christie, M.J., Napier, I.A., et al. (2010). Dendritic function of tau mediates amyloid-beta toxicity in Alzheimer's disease mouse models. Cell *142*, 387–397.

Kapus, A., Szászi, K., Sun, J., Rizoli, S., and Rotstein, O.D. (1999). Cell shrinkage regulates Src kinases and induces tyrosine phosphorylation of cortactin, independent of the osmotic regulation of Na^+/H^+ exchangers. J. Biol. Chem. *274*, 8093–8102.

Kaufman, A.C., Salazar, S.V., Haas, L.T., Yang, J., Kostylev, M.A., Jeng, A.T., Robinson, S.A., Gunther, E.C., van Dyck, C.H., Nygaard, H.B., and Strittmatter, S.M. (2015). Fyn inhibition rescues established memory and synapse loss in Alzheimer mice. Ann. Neurol. *77*, 953–971.

Köhler, C., Fuhr, V., and Dinekov, M. (2017). Distribution of spleen tyrosine kinase and tau phosphorylated at tyrosine 18 in a mouse model of tauopathy and in the human hippocampus. Brain Res. *1677*, 1–13.

Kojima, N., Wang, J., Mansuy, I.M., Grant, S.G.N., Mayford, M., and Kandel, E.R. (1997). Rescuing impairment of long-term potentiation in fyn-deficient mice by introducing Fyn transgene. Proc. Natl. Acad. Sci. USA *94*, 4761–4765.

Kuchibhotla, K.V., Wegmann, S., Kopeikina, K.J., Hawkes, J., Rudinskiy, N., Andermann, M.L., Spires-Jones, T.L., Bacskai, B.J., and Hyman, B.T. (2014). Neurofibrillary tangle-bearing neurons are functionally integrated in cortical circuits in vivo. Proc. Natl. Acad. Sci. USA *111*, 510–514.

Lambert, M.P., Barlow, A.K., Chromy, B.A., Edwards, C., Freed, R., Liosatos, M., Morgan, T.E., Rozovsky, I., Trommer, B., Viola, K.L., et al. (1998). Diffusible, nonfibrillar ligands derived from Abeta1-42 are potent central nervous system neurotoxins. Proc. Natl. Acad. Sci. USA *95*, 6448–6453.

Larson, M., Sherman, M.A., Amar, F., Nuvolone, M., Schneider, J.A., Bennett, D.A., Aguzzi, A., and Lesné, S.E. (2012). The complex PrP(c)-Fyn couples human oligomeric Aβ with pathological tau changes in Alzheimer's disease. J. Neurosci. *32*, 16857–16871.

Lasagna-Reeves, C.A., Castillo-Carranza, D.L., Sengupta, U., Clos, A.L., Jackson, G.R., and Kayed, R. (2011). Tau oligomers impair memory and induce synaptic and mitochondrial dysfunction in wild-type mice. Mol. Neurodegener. *6*, 39.

Lau, D.H., Hogseth, M., Phillips, E.C., O'Neill, M.J., Pooler, A.M., Noble, W., and Hanger, D.P. (2016). Critical residues involved in tau binding to fyn: implications for tau phosphorylation in Alzheimer's disease. Acta Neuropathol. Commun. *4*, 49.

Laurent, C., Buée, L., and Blum, D. (2018). Tau and neuroinflammation: what impact for Alzheimer's disease and tauopathies? Biomed. J. *41*, 21–33.

Lee, G., Newman, S.T., Gard, D.L., Band, H., and Panchamoorthy, G. (1998). Tau interacts with src-family non-receptor tyrosine kinases. J. Cell Sci. *111*, 3167–3177.

Lee, G., Thangavel, R., Sharma, V.M., Litersky, J.M., Bhaskar, K., Fang, S.M., Do, L.H., Andreadis, A., Van Hoesen, G., and Ksiezak-Reding, H. (2004). Phosphorylation of tau by fyn: implications for Alzheimer's disease. J. Neurosci. *24*, 2304–2312.

Lee, C., Low, C.Y.B., Wong, S.Y., Lai, M.K.P., and Tan, M.G.K. (2017). Selective induction of alternatively spliced FynT isoform by TNF facilitates persistent inflammatory responses in astrocytes. Sci. Rep. *7*, 43651.

Lesort, M., Jope, R.S., and Johnson, G.V. (1999). Insulin transiently increases tau phosphorylation: involvement of glycogen synthase kinase-3beta and Fyn tyrosine kinase. J. Neurochem. *72*, 576–584.

Li, C., and Götz, J. (2017). Somatodendritic accumulation of Tau in Alzheimer's disease is promoted by Fyn-mediated local protein translation. EMBO J. *36*, 3120–3138.

Li, C., and Götz, J. (2018). Pyk2 is a novel tau tyrosine kinase that is regulated by the tyrosine kinase Fyn. J. Alzheimers Dis. *64*, 205–221.

Li, P., Banjade, S., Cheng, H.C., Kim, S., Chen, B., Guo, L., Llaguno, M., Hollingsworth, J.V., King, D.S., Banani, S.F., et al. (2012). Phase transitions in the assembly of multivalent signalling proteins. Nature *483*, 336–340.

Li, C., Briner, A., and Götz, J. (2019). The search for improved animal models of Alzheimer's disease and novel strategies for therapeutic intervention. Future Med. Chem. *11*, 1853–1857.

Lin, Y., Fichou, Y., Zeng, Z., Hu, N.Y., and Han, S. (2020). Electrostatically driven complex coacervation and amyloid aggregation of tau are independent processes with overlapping conditions. ACS Chem. Neurosci. *11*, 615–627.

Mackenzie, I.R., Nicholson, A.M., Sarkar, M., Messing, J., Purice, M.D., Pottier, C., Annu, K., Baker, M., Perkerson, R.B., Kurti, A., et al. (2017). TIA1 mutations in amyotrophic lateral sclerosis and frontotemporal dementia promote phase separation and alter stress granule dynamics. Neuron *95*, 808–816.e9.

Mann, J.R., Gleixner, A.M., Mauna, J.C., Gomes, E., DeChellis-Marks, M.R., Needham, P.G., Copley, K.E., Hurtle, B., Portz, B., Pyles, N.J., et al. (2019). RNA binding antagonizes neurotoxic phase transitions of TDP-43. Neuron *102*, 321–338.e8.

Martin, L., Latypova, X., Wilson, C.M., Magnaudeix, A., Perrin, M.-L., Yardin, C., and Terro, F. (2013). Tau protein kinases: involvement in Alzheimer's disease. Ageing Res. Rev. *12*, 289–309.

Maziuk, B.F., Apicco, D.J., Cruz, A.L., Jiang, L., Ash, P.E.A., da Rocha, E.L., Zhang, C., Yu, W.H., Leszyk, J., Abisambra, J.F., et al. (2018). RNA binding proteins co-localize with small tau inclusions in tauopathy. Acta Neuropathol. Commun. *6*, 71.

Minami, S.S., Clifford, T.G., Hoe, H.S., Matsuoka, Y., and Rebeck, G.W. (2012). Fyn knock-down increases Abeta, decreases phospho-tau, and worsens spatial learning in 3xTg-AD mice. Neurobiol. Aging *33*, 825.e815–824.

Mirbaha, H., Chen, D., Morazova, O.A., Ruff, K.M., Sharma, A.M., Liu, X., Goodarzi, M., Pappu, R.V., Colby, D.W., Mirzaei, H., et al. (2018). Inert and seed-competent tau monomers suggest structural origins of aggregation. eLife *7*, e36584.

Miyamoto, T., Stein, L., Thomas, R., Djukic, B., Taneja, P., Knox, J., Vossel, K., and Mucke, L. (2017). Phosphorylation of tau at Y18, but not tau-fyn binding, is required for tau to modulate NMDA receptor-dependent excitotoxicity in primary neuronal culture. Mol. Neurodegener. *12*, 41.

Molliex, A., Temirov, J., Lee, J., Coughlin, M., Kanagaraj, A.P., Kim, H.J., Mittag, T., and Taylor, J.P. (2015). Phase separation by low complexity domains promotes stress granule assembly and drives pathological fibrillization. Cell *163*, 123–133.

Motulsky, H.J., and Brown, R.E. (2006). Detecting outliers when fitting data with nonlinear regression - a new method based on robust nonlinear regression and the false discovery rate. BMC Bioinformatics *7*, 123.

Mukrasch, M.D., Bibow, S., Korukottu, J., Jeganathan, S., Biernat, J., Griesinger, C., Mandelkow, E., and Zweckstetter, M. (2009). Structural polymorphism of 441-residue tau at single residue resolution. PLoS Biol. *7*, e34.

Narasimhan, S., Guo, J.L., Changolkar, L., Stieber, A., McBride, J.D., Silva, L.V., He, Z., Zhang, B., Gathagan, R.J., Trojanowski, J.Q., and Lee, V.M.Y. (2017). Pathological tau strains from human brains recapitulate the diversity of tauopathies in nontransgenic mouse brain. J. Neurosci. *37*, 11406–11423.

Narayanan, A., Meriin, A., Andrews, J.O., Spille, J.-H., Sherman, M.Y., and Cisse, I.I. (2019). A first order phase transition mechanism underlies protein aggregation in mammalian cells. eLife *8*, e39695.

Neddens, J., Temmel, M., Flunkert, S., Kerschbaumer, B., Hoeller, C., Loeffler, T., Niederkofler, V., Daum, G., Attems, J., and Hutter-Paier, B. (2018). Phosphorylation of different tau sites during progression of Alzheimer's disease. Acta Neuropathol. Commun. *6*, 52.

Nelson, P.T., Alafuzoff, I., Bigio, E.H., Bouras, C., Braak, H., Cairns, N.J., Castellani, R.J., Crain, B.J., Davies, P., Del Tredici, K., et al. (2012). Correlation of Alzheimer disease neuropathologic changes with cognitive status: a review of the literature. J. Neuropathol. Exp. Neurol. *71*, 362–381.

Nott, T.J., Petsalaki, E., Farber, P., Jervis, D., Fussner, E., Plochowietz, A., Craggs, T.D., Bazett-Jones, D.P., Pawson, T., Forman-Kay, J.D., and Baldwin, A.J. (2015). Phase transition of a disordered nuage protein generates environmentally responsive membraneless organelles. Mol. Cell *57*, 936–947.

Nygaard, H.B. (2018). Targeting Fyn kinase in Alzheimer's disease. Biol. Psychiatry *83*, 369–376.

Ohnishi, H., Murata, Y., Okazawa, H., and Matozaki, T. (2011). Src family kinases: modulators of neurotransmitter receptor function and behavior. Trends Neurosci. *34*, 629–637.

Padmanabhan, P., Martínez-Mármol, R., Xia, D., Götz, J., and Meunier, F.A. (2019). Frontotemporal dementia mutant Tau promotes aberrant Fyn nanoclustering in hippocampal dendritic spines. eLife *8*, e45040.

Panicker, N., Saminathan, H., Jin, H., Neal, M., Harischandra, D.S., Gordon, R., Kanthasamy, K., Lawana, V., Sarkar, S., Luo, J., et al. (2015). Fyn kinase regulates microglial neuroinflammatory responses in cell culture and animal models of Parkinson's disease. J. Neurosci. *35*, 10058–10077.

Patel, A., Lee, H.O., Jawerth, L., Maharana, S., Jahnel, M., Hein, M.Y., Stoynov, S., Mahamid, J., Saha, S., Franzmann, T.M., et al. (2015). A liquid-to-solid phase transition of the ALS protein FUS accelerated by disease mutation. Cell *162*, 1066–1077.

Polanco, J.C., Scicluna, B.J., Hill, A.F., and Götz, J. (2016). Extracellular vesicles isolated from the brains of rTg4510 mice seed tau protein aggregation in a threshold-dependent manner. J. Biol. Chem. *291*, 12445–12466.

Polanco, J.C., Li, C., Bodea, L.G., Martinez-Marmol, R., Meunier, F.A., and Götz, J. (2018a). Amyloid-β and tau complexity - towards improved biomarkers and targeted therapies. Nat. Rev. Neurol. *14*, 22–39.

Polanco, J.C., Li, C., Durisic, N., Sullivan, R., and Götz, J. (2018b). Exosomes taken up by neurons hijack the endosomal pathway to spread to interconnected neurons. Acta Neuropathol. Commun. *6*, 10.

Roberson, E.D., Scearce-Levie, K., Palop, J.J., Yan, F., Cheng, I.H., Wu, T., Gerstein, H., Yu, G.Q., and Mucke, L. (2007). Reducing endogenous tau ameliorates amyloid beta-induced deficits in an Alzheimer's disease mouse model. Science *316*, 750–754.

Roux, P.P., Shahbazian, D., Vu, H., Holz, M.K., Cohen, M.S., Taunton, J., Sonenberg, N., and Blenis, J. (2007). RAS/ERK signaling promotes site-specific ribosomal protein S6 phosphorylation via RSK and stimulates cap-dependent translation. J. Biol. Chem. *282*, 14056–14064.

Salmond, R.J., Emery, J., Okkenhaug, K., and Zamoyska, R. (2009). MAPK, phosphatidylinositol 3-kinase, and mammalian target of rapamycin pathways converge at the level of ribosomal protein S6 phosphorylation to control metabolic signaling in CD8 T cells. J. Immunol. *183*, 7388–7397.

Sanders, D.W., Kaufman, S.K., DeVos, S.L., Sharma, A.M., Mirbaha, H., Li, A., Barker, S.J., Foley, A.C., Thorpe, J.R., Serpell, L.C., et al. (2014). Distinct tau prion strains propagate in cells and mice and define different tauopathies. Neuron *82*, 1271–1288.

Santacruz, K., Lewis, J., Spires, T., Paulson, J., Kotilinek, L., Ingelsson, M., Guimaraes, A., DeTure, M., Ramsden, M., McGowan, E., et al. (2005). Tau suppression in a neurodegenerative mouse model improves memory function. Science *309*, 476–481.

Sasaki, Y., Cheng, C., Uchida, Y., Nakajima, O., Ohshima, T., Yagi, T., Taniguchi, M., Nakayama, T., Kishida, R., Kudo, Y., et al. (2002). Fyn and Cdk5 mediate semaphorin-3A signaling, which is involved in regulation of dendrite orientation in cerebral cortex. Neuron *35*, 907–920.

Shelton, L.B., Baker, J.D., Zheng, D., Sullivan, L.E., Solanki, P.K., Webster, J.M., Sun, Z., Sabbagh, J.J., Nordhues, B.A., Koren, J., 3rd., et al. (2017). Hsp90 activator Aha1 drives production of pathological tau aggregates. Proc. Natl. Acad. Sci. USA *114*, 9707–9712.

Shin, Y., and Brangwynne, C.P. (2017). Liquid phase condensation in cell physiology and disease. Science *357*, eaaf4382.

Shoffner, S.K., and Schnell, S. (2016). Estimation of the lag time in a subsequent monomer addition model for fibril elongation. Phys. Chem. Chem. Phys. *18*, 21259–21268.

Stöhr, J., Wu, H., Nick, M., Wu, Y., Bhate, M., Condello, C., Johnson, N., Rodgers, J., Lemmin, T., Acharya, S., et al. (2017). A 31-residue peptide induces aggregation of tau's microtubule-binding region in cells. Nat. Chem. *9*, 874–881.

Takeda, S., Wegmann, S., Cho, H., DeVos, S.L., Commins, C., Roe, A.D., Nicholls, S.B., Carlson, G.A., Pitstick, R., Nobuhara, C.K., et al. (2015). Neuronal uptake and propagation of a rare phosphorylated high-molecular-weight tau derived from Alzheimer's disease brain. Nat. Commun. *6*, 8490.

Tan, R., Lam, A.J., Tan, T., Han, J., Nowakowski, D.W., Vershinin, M., Simó, S., Ori-McKenney, K.M., and McKenney, R.J. (2019). Microtubules gate tau condensation to spatially regulate microtubule functions. Nat. Cell Biol. *21*, 1078–1085.

Trepanier, C.H., Jackson, M.F., and MacDonald, J.F. (2012). Regulation of NMDA receptors by the tyrosine kinase Fyn. FEBS J. *279*, 12–19.

Um, J.W., Nygaard, H.B., Heiss, J.K., Kostylev, M.A., Stagi, M., Vortmeyer, A., Wisniewski, T., Gunther, E.C., and Strittmatter, S.M. (2012). Alzheimer amyloid-β oligomer bound to postsynaptic prion protein activates Fyn to impair neurons. Nat. Neurosci. *15*, 1227–1235.

Um, J.W., Kaufman, A.C., Kostylev, M., Heiss, J.K., Stagi, M., Takahashi, H., Kerrisk, M.E., Vortmeyer, A., Wisniewski, T., Koleske, A.J., et al. (2013). Metabotropic glutamate receptor 5 is a coreceptor for Alzheimer aβ oligomer bound to cellular prion protein. Neuron *79*, 887–902.

Umemori, H., Sato, S., Yagi, T., Aizawa, S., and Yamamoto, T. (1994). Initial events of myelination involve Fyn tyrosine kinase signalling. Nature *367*, 572–576.

Usardi, A., Pooler, A.M., Seereeram, A., Reynolds, C.H., Derkinderen, P., Anderton, B., Hanger, D.P., Noble, W., and Williamson, R. (2011). Tyrosine phosphorylation of tau regulates its interactions with Fyn SH2 domains, but not SH3 domains, altering the cellular localization of tau. FEBS J. *278*, 2927–2937.

Vanderweyde, T., Apicco, D.J., Youmans-Kidder, K., Ash, P.E.A., Cook, C., Lummertz da Rocha, E., Jansen-West, K., Frame, A.A., Citro, A., Leszyk, J.D., et al. (2016). Interaction of tau with the RNA-binding protein TIA1 regulates tau pathophysiology and toxicity. Cell Rep. *15*, 1455–1466.

Wang, Y., and Mandelkow, E. (2016). Tau in physiology and pathology. Nat. Rev. Neurosci. *17*, 5–21.

Wang, J., Choi, J.-M., Holehouse, A.S., Lee, H.O., Zhang, X., Jahnel, M., Maharana, S., Lemaitre, R., Pozniakovsky, A., Drechsel, D., et al. (2018). A molecular grammar governing the driving forces for phase separation of prion-like RNA binding proteins. Cell *174*, 688–699.e16.

Ward, S.M., Himmelstein, D.S., Lancia, J.K., Fu, Y., Patterson, K.R., and Binder, L.I. (2013). TOC1: characterization of a selective oligomeric tau antibody. J. Alzheimers Dis. *37*, 593–602.

Wegmann, S., Eftekharzadeh, B., Tepper, K., Zoltowska, K.M., Bennett, R.E., Dujardin, S., Laskowski, P.R., MacKenzie, D., Kamath, T., Commins, C., et al. (2018). Tau protein liquid-liquid phase separation can initiate tau aggregation. EMBO J *37*, e98049.

Wu, J.W., Hussaini, S.A., Bastille, I.M., Rodriguez, G.A., Mrejeru, A., Rilett, K., Sanders, D.W., Cook, C., Fu, H., Boonen, R.A., et al. (2016). Neuronal activity enhances tau propagation and tau pathology in vivo. Nat. Neurosci. *19*, 1085–1092.

Xia, D., and Götz, J. (2014). Premature lethality, hyperactivity, and aberrant phosphorylation in transgenic mice expressing a constitutively active form of Fyn. Front. Mol. Neurosci. *7*, 40.

Xia, D., Li, C., and Götz, J. (2015). Pseudophosphorylation of Tau at distinct epitopes or the presence of the P301L mutation targets the microtubule-associated protein Tau to dendritic spines. Biochim. Biophys. Acta *1852*, 913–924.

Yamada, K., Holth, J.K., Liao, F., Stewart, F.R., Mahan, T.E., Jiang, H., Cirrito, J.R., Patel, T.K., Hochgräfe, K., Mandelkow, E.M., and Holtzman, D.M. (2014). Neuronal activity regulates extracellular tau in vivo. J. Exp. Med. *211*, 387–393.

Yoshiyama, Y., Higuchi, M., Zhang, B., Huang, S.M., Iwata, N., Saido, T.C., Maeda, J., Suhara, T., Trojanowski, J.Q., and Lee, V.M. (2007). Synapse loss and microglial activation precede tangles in a P301S tauopathy mouse model. Neuron *53*, 337–351.

Zhang, X., Lin, Y., Eschmann, N.A., Zhou, H., Rauch, J.N., Hernandez, I., Guzman, E., Kosik, K.S., and Han, S. (2017). RNA stores tau reversibly in complex coacervates. PLoS Biol. *15*, e2002183.

STAR★METHODS

KEY RESOURCES TABLE

REAGENT or RESOURCE	SOURCE	IDENTIFIER
Antibodies		
Mouse monoclonal anti-oligomeric tau TOC1, 1:10000 DB	Dr Nicholas Kanaan	N/A
Rabbit monoclonal anti-GAPDH, 1:1000 DB	Millipore	#ABS16; RRID: AB_10806772
Mouse monoclonal anti-tau pY18, 1:1000 IF and IB	Medimabs	#MM0194P
Mouse monoclonal anti-tau AT8, 1:500 IHC, 1:1000 IB	Thermo Fisher	#MN1020; RRID: AB_223648
Mouse monoclonal anti-tau AT180, 1:500 IHC, 1:1000 IB	Thermo Fisher	#MN1040; RRID: AB_223649
Mouse monoclonal anti-tau Tau5, 1:5000 IB	Thermo Fisher	#AHB0042; RRID: AB_2536235
Mouse monoclonal anti-tau HT7, 1:5000 IB	Thermo Fisher	#MN1000; RRID: AB_2314654
Rabbit polyclonal anti-Fyn, 1:1000 IB	Cell Signaling Technology	#4023; RRID: AB_10698604
Mouse monoclonal anti-GFAP, 1:500 IF	Millipore	#MAB360; RRID: AB_11212597
Rabbit monoclonal anti-Iba1, 1:500 IF	Wako	#016-26721; RRID: AB_2811160
Goat-anti-mouse Alexa Fluor 488 secondary antibody, 1:500 IF	Thermo Fisher	#A11001; RRID: AB_2534069
Goat-anti-rabbit Alexa Fluor 647 secondary antibody, 1:500 IF	Thermo Fisher	#A21245; RRID: AB_2535813
Rabbit-anti-mouse biotinylated secondary antibody, 1:500 IHC	Dako	#E0413
Goat-anti-mouse IR Dye 800CW, 1:10000 IB	LI-COR	#926-32210; RRID: AB_621842
Goat-anti-mouse IR Dye 680RD, 1:10000 IB	LI-COR	#926-68070; RRID: AB_10956588
Goat-anti-rabbit IR Dye 800CW, 1:10000 IB	LI-COR	#926-32211; RRID: AB_621843
Goat-anti-rabbit IR Dye 680RD, 1:10000 IB	LI-COR	#926-68071; RRID: AB_10956166
Goat-anti-mouse IgM IR Dye 800CW, 1:10000 IB	LI-COR	#925-32280
Mouse monoclonal anti-p44/42 MAPK (Erk1/2), 1:2000 IB	Cell Signaling Technology	#4696; RRID: AB_390780
Rabbit monoclonal anti-phospho-Erk1/2 (Thr202/Tyr204), IB 1:2000	Cell Signaling Technology	#4370; RRID: AB_2315112
Bacterial and Virus Strains		
BL21(DE3)	New England Biolabs	#C2527I
Biological Samples		
Chemicals, Peptides, and Recombinant Proteins		
3, 3′-diaminobenzidine (DAB)	Dako	#K3468
RAB buffer	G Biosciences	786-91
RIPA buffer	Cell Signaling Technology	#9806
Recombinant hTau	This paper	N/A
Recombinant hTau-Y18E	This paper	N/A
Recombinant hTau-Y18A	This paper	N/A
Heparin	Sigma	#H3393
Thioflavin T	Sigma	#T3516
Critical Commercial Assays		
VECTAstain ABC HRP Kit	Vector Laboratories	#PK4000; RRID:AB_2336818
DC Protein Assay	Bio-Rad	#5000112
REVERT 700 Total Protein Stain	LI-COR	#926-11011
Deposited Data		
Experimental Models: Cell Lines		
HEK293T	ATCC	CRL-3216; RRID:CVCL_0063
Tau RD-CFP	Dr Michael Diamond	N/A

(*Continued on next page*)

Continued

REAGENT or RESOURCE	SOURCE	IDENTIFIER
Tau RD-YFP	Dr Michael Diamond	N/A
FRET tau RD-CFP RD-YFP biosensor cell	Dr Michael Diamond	N/A
Experimental Models: Organisms/Strains		
rTg4510 (0N4R-P301L-tau) mouse	The Jackson Laboratory	JAX:024854; RRID:IMSR_JAX:024854
129-Fyntm1Sor/J (Fyn-knockout) mouse	The Jackson Laboratory	JAX:002271; RRID:IMSR_JAX:002271
Tg/Fyn$^{-/-}$ mouse	This paper	N/A
Oligonucleotides		
hTau-Y18E site-directed mutagenesis FW primer: CGCTGGG ACGGAAGGGTTGGGGGAC	This paper	N/A
hTau-Y18A site-directed mutagenesis FW primer: CGCTGG GACGGCCGGGTTGGGGGAC	This paper	N/A
hTau site directed mutagenesis RV primer: TGATCTTCCAT CACTTCGAACTCCTGGC	This paper	N/A
hTau/Y18E/Y18A LIC FW primer: TACTTCCAATCCAATGCAA TGGCTGAGCCCCGCCAG	This paper	N/A
hTau/Y18E/Y18A LIC FW primer: TTATCCACTTCCAATGTT ATTACAAACCCTGCTTGGCCAG	This paper	N/A
Recombinant DNA		
pET-His6-TEV-LIC vector 1B	Scott Gradia	Addgene #29653; RRID:Addgene_29653
pENTR hTau 441aa	Xia et. al., 2015	N/A
hTau-pET-His6-TEV-LIC	This paper	N/A
Tau-Y18E-pET-His6-TEV-LIC	This paper	N/A
Tau-Y18A-pET-His6-TEV-LIC	This paper	N/A
Software and Algorithms		
ImageJ (FIJI)	NIH	https://fiji.sc/
Prism 8.0	GraphPad	https://www.graphpad.com/scientific-software/prism/
LI-COR Image Studio	LI-COR	https://www.licor.com/bio/image-studio/
FlowJo xV software	Tree Star	https://www.flowjo.com/solutions/flowjo
ImageJ histology percentage area quantification macro	This paper	GitHub; https://github.com/QBI-Software

RESOURCE AVAILABILITY

Lead contact

Further information and requests for resources and reagents should be directed to and will be fulfilled by the Lead Contact, Juan Carlos Polanco (j.polanco@uq.edu.au).

Materials availability

All unique resources generated in this study are available from the Lead Contact with a completed Materials Transfer Agreement.

Data and Code Availability

Custom ImageJ scripts used in the analysis of histological images generated during this study are available at GitHub [https://github.com/QBI-Software]. Original data generated by this study are available upon request.

EXPERIMENTAL MODEL AND SUBJECT DETAILS

Animals

rTg4510 mice, which express 0N4R human tau with the FTLD-associated P301L mutation (Santacruz et al., 2005), and homozygous Fyn-knockout mice (Grant et al., 1992) were obtained from Jackson Laboratories, and backcrossed for >5 generations onto the C57BL/6 background. The novel Tg/Fyn$^{-/-}$ strain was generated by crossing rTg4510 with Fyn-knockout mice until the homozygosity of the knockout within the progeny was reached. The genotype of all mice was confirmed by sequencing and each mouse was

re-genotyped after sacrificing. All mice were used at 6 months of age, at which point the rTg4510 strain displays significant tau pathology and neuronal loss (Santacruz et al., 2005). Fyn-knockout and Tg/Fyn$^{-/-}$ mice maintained on the C57BL/6 background display obstructive hydrocephalus, a phenotype observed in our hands with a penetrance of ~25% (Goto et al., 2008). We made significant efforts to exclude such mice from our analyses.

Gender-matched (n = 4 male and females each) rTg4510 mice, wild-type (WT) littermates, and Tg/Fyn$^{-/-}$ mice were used for histological analyses. Biochemical analyses and lysates used in the treatment of biosensor cells (n = 3 or 5, depending on the experiment) were performed with female mice only due to availability constraints. Animals were housed in pathogen-free cages and maintained on a 12 h light/dark cycle, with *ad libitum* access to food and water. Experiments were approved by the Animal Ethics Committee of the University of Queensland (approval numbers QBI/412/14/NHMRC and QBI/554/17/NHMRC).

Cell culture

Modified HEK293T cell lines (generously provided by Dr Marc Diamond, UT Southwestern Medical Center, USA) were used for tau aggregation experiments, while unmodified HEK293T (ATCC, CRL-3216) were used for retroviral production. Two fluorophore-control polyclonal cell lines, stably expressing tau repeat domain (RD)-CFP or RD-YFP, were used alongside a monoclonal FRET tau biosensor cell line that expresses both RD-CFP and RD-YFP (Holmes et al., 2014). All cell lines were grown in DMEM (Life Technologies, #11965092) supplemented with 5% FBS (Scientifix Life, #FFBS500), 2mM GlutaMAX (Life Technologies, #35050061), 100 units/ml penicillin and 100 μg/ml streptomycin (Life Technologies, #15140122) at 37°C and 5% CO_2.

METHOD DETAILS

Behavioral analyses and brain mass measurements

Mice were subjected to active place avoidance (APA) test using a six-day paradigm. Briefly, the animals were handled for 2 min each day for the week prior to behavioral testing. The APA arena consisted of a rotating (1 rpm), elevated, circular arena with a grid metal floor fenced by clear Perspex, with four A3-sized black-and-white visual cues hung from the four surrounding walls. The specific cues did not change over the course of the experiment. Mice were habituated in the arena one day prior to the first experimental day for 10 min. On experimental days 1-6, mice (tracked by an overhead camera) which entered into a 60 sector of the arena aligned with a given visual cue (the position of which did not change in relation to the room), received a footshock (0.5mA, 500ms, 60 Hz, 1.5 s intervals), driven by Track Analysis software (Bio-Signal Group). The animals always entered the arena opposite the footshock zone, and the arena was thoroughly cleaned between mice. Males were run on separate days to females to further prevent any possible scent distraction. The total number of entrances to the shock zone, total distance covered, and time to first and second entrances were recorded over the 10-minute session using Track Analysis software.

Open-field activity monitors were used to analyze baseline locomotion and assess for anxiety phenotypes (Belzung and Griebel, 2001). Mice were placed into the center of roughly cubic (27.5 cm x 27.5 cm x 30 cm high) clear Perspex arenas, each of which contained two arrays of 16 × 16 infrared beams. One of these arrays was positioned ~1 cm above the floor so that beams were broken when the mouse was moving laterally; the other was positioned ~8 cm above the floor, so that beams would be broken when the animal reared. Mice were tracked throughout a 30 min session, in which they were allowed to freely ambulate and explore. Mouse position data were automatically calculated and tracked with EthoVision® software (Noldus, Sydney, NSW, AUS). Data were binned into 5 min blocks, and a center zone comprising a central square of size half the length and breadth of the arena was defined. The number of center entries, the time spent in the center zone, and the total distance traveled per bin were recorded.

Mouse coordination and equilibrium were analyzed using an accelerating Rotarod (Ugo Basile). Mice were placed on the Rotarod apparatus in acceleration mode for 180 s (accelerating linearly from 3-30 rpm over 90 s, maintained at 30 rpm for 90 s). Each mouse was trialled three times, and the median latency to fall off the rod was recorded.

Brain mass of WT, rTg4510 and Tg/Fyn$^{-/-}$ mice was recorded immediately after perfusion and excision from 6-month-old mice, as described below for immunostaining and biochemical analyses. A total of 20 mice (10 males and 10 females) were measured; datasets were merged after no significant differences were found between male and female mice of the same strain in terms of brain mass. For each mouse, the entire cerebrum (with cerebellum still attached) was weighed.

Immunohistochemistry and immunofluorescence

Immunohistochemistry and immunofluorescence of phospho-tau species were performed as described previously with minor modifications (Baker et al., 2016). Briefly, mice were anesthetized and perfused transcardially with phosphate-buffered saline (PBS, pH 7.4). The whole brains were then immersion fixed overnight in 4% paraformaldehyde (PFA) in PBS at 4°C, dehydrated by ethanol series and embedded in paraffin. Serial coronal sections were cut at 7μm with a microtome and mounted onto Superfrost Plus slides (Menzel-Gläser, #SF41296SP). Sections were rehydrated in accordance with standard protocols and boiled in citrate buffer (pH 5.8) for 15 min using a microwave. After cooling, sections were blocked for 1 h in 1% BSA and 20% FBS in Tris-buffered saline (TBS, pH 7.4) with 0.05% Triton X-100 (Sigma, #T8787) and then incubated overnight at 4°C with primary antibodies diluted in blocking buffer.

For immunohistochemistry of paraffin sections, after incubation with primary antibodies sections were washed with 3% H_2O_2 in TBS to quench endogenous peroxidase activity, then incubated with biotinylated secondary antibodies (Dako, #E0413, 1:500 dilution) for 1.5 h at room temperature. Immunodetection was subsequently performed with 3, 3′-diaminobenzidine (DAB) chromogen

(Dako, #K3468) following treatment with streptavidin-horseradish peroxidase ABC reagent (Vector Laboratories, #PK4000). Sections were counterstained with hematoxylin to provide cytological detail. For immunofluorescence of paraffin sections, Alexa Fluor 488-labeled goat-anti-mouse IgG secondary antibodies (Thermo Fisher, #A11001, 1:500 dilution) were used, together with DAPI (0.1μg/ml) counterstaining for nuclei. Gallyas silver staining for the detection of tau neurofibrillary tangles (NFTs) was performed as previously reported (Baker et al., 2016) using standard histological techniques

For glial stainings, immunofluorescence was conducted with free-floating 40μm sections cut by a vibratome (Leica). Sections were blocked in a blocking buffer comprising 5% BSA in PBS with 0.2% Triton-X at room temperature for 1 h, and subsequently incubated with primary antibodies against GFAP (Millipore, #MAB360) and Iba1 (Wako, #016-26721, both diluted to 1:500) in the same buffer supplemented with 0.02% sodium azide for 72 h. Sections were washed thrice in PBS and then probed with the appropriate Alexa Fluor 488- and 647-conjugated secondary antibodies (Thermo Fisher, # A21245, both used at 1:500 dilution) in PBS with 0.2% Triton-X at room temperature for 1 h. Sections were washed as above, incubated with DAPI and mounted.

For paraffin immunohistochemistry and immunofluorescence, tissue sections were imaged with brightfield or fluorescence slide scanners (Zeiss) at 10x and 20x, respectively. Glial staining was imaged using a spinning-disk confocal system (Marianas; 3I, Inc.) consisting of an Axio Observer Z1 (Carl Zeiss) equipped with a CSU-W1 spinning-disk head (Yokogawa Corporation of America), ORCA-Flash4.0 v2 sCMOS camera (Hamamatsu Photonics), and 63x 1.4 NA PlanApo oil immersion objective, with image acquisition, performed using SlideBook 6.0 (3I, Inc).

Whole-brain RAB-RIPA/SDS fractionation

Brains were dissected from mice transcardially perfused with PBS, and then snap-frozen in liquid nitrogen. For fractionation, the brains were immersed in six volumes of RAB buffer (G-Biosciences, #78691) with protease and phosphatase inhibitors and homogenized using the TissueLyser LT (QIAGEN) for a total of 6 min at 50Hz. Homogenates were then centrifuged at 21,000*g* for 90 min at 4°C and the supernatant was stored at −80°C as the RAB-soluble fraction. The pellet was homogenized as above with the TissueLyser LT in the same volume of RIPA buffer (Cell Signaling Technology, #9806) supplemented with 1% SDS, protease and phosphatase inhibitors, and then spun again as before. The RIPA/SDS-soluble supernatant was retained and stored at −80°C.

Synaptosomal fractionation

Synaptosomal fractionation was performed as reported previously with minor amendments (D'Amelio et al., 2011). Mice were anesthetized and perfused with cold Hank's balanced salt solution (HBSS, pH 7.4, Life Technologies, #14185052), and brains were quickly homogenized by hand with 15 strokes of a tight-fitting Dounce tissue grinder in homogenization buffer (320mM sucrose, 4mM HEPES, pH 7.4) supplemented with protease and phosphatase inhibitors. The homogenate was centrifuged at 1,000*g* at 4°C for 10 min, and the resulting supernatant was centrifuged at 12,000*g* for 15 min. The resulting pellet was resuspended in homogenization buffer, and centrifuged at 13,000*g* for 15 min to obtain the final synaptosome-enriched pellet, which was snap-frozen on dry ice and stored at −80°C.

To prepare synaptosomal fractions for biochemical analyses, the synaptosome-enriched pellet was resuspended in 250μl of RAB buffer with protease and phosphatase inhibitors, briefly sonicated, and then spun at 10,000*g* for 20 min at 4°C. The supernatant was snap-frozen and retained as the RAB-soluble synaptosome. The RAB-insoluble pellet was then resuspended in 250μl of RIPA buffer supplemented with 1% SDS and protease and phosphatase inhibitors, sonicated, and centrifuged as above, thereby generating a RIPA/SDS-soluble synaptosome that was snap-frozen and stored at −80°C.

PBS brain lysates

To generate PBS lysates used in tau biosensor cell and dot-blot experiments, brains were Dounce homogenized in PBS with protease and phosphatase inhibitors with 15 strokes of an electric drill. Samples were kept on ice for 15 min and then spun at 10,000*g* for 15 min for tau seeding experiments, or 3,000*g* for 5 min for dot-blot analysis (both at 4°C). In each case, the resulting supernatant was snap-frozen and stored at −80°C until use.

Immunoblot and dot-blot

Brain extracts were quantified by DC assay (Bio-Rad, #5000112) and 20μg of protein were boiled for 5 min in sample buffer (125mM Tris-HCl pH 6.8, 2% SDS, 12.5% glycerol, 90mM DTT) and resolved by SDS-PAGE on 7.5% polyacrylamide gels in Tris-glycine-SDS buffer (Bio-Rad, #1610732). Gels were transferred using the Trans-Blot Turbo Transfer System (Bio-Rad, #1704150) to low-fluorescence PVDF membranes (Bio-Rad, #1620263) and total protein staining for normalization was performed with REVERT Total Protein Stain Kit (LI-COR, #926-11010) in accordance with the manufacturer's instructions. Membranes were blocked with Odyssey blocking buffer (LI-COR, #927-5000) at room temperature for 1 h and subsequently reacted with primary antibodies diluted in Odyssey block with 0.1% Tween-20 (Sigma, #P1379) overnight at 4°C with gentle rocking. After washing thrice for 5 min in TBS with 0.05% Tween-20 (TBS-T), membranes were probed with complementary IR Dye 680RD/800CW secondary IgG antibodies (LI-COR, #925-32210, #925-68070, #925-32211, #925-68071, 1:10,000 dilution in a buffer of 1:1 Odyssey block and TBS-T) for 1 h at room temperature. After washing again in TBS-T, membranes were rinsed briefly in TBS and scanned with the Odyssey Fc Imaging System (LI-COR) to detect infrared signal.

For dot-blotting, PBS brain lysates containing 18μg of protein (quantified as above) were diluted in 100μl of PBS and adsorbed slowly onto moistened 0.45μm nitrocellulose membranes (Millipore, #HATF00010), followed by washing with PBS by vacuum using a Bio-Dot apparatus (Bio-Rad, #170-6545). Membranes were then blocked as above and probed with anti-oligomeric tau antibody TOC1 (a generous gift of Dr Nicholas Kanaan, used 1:10000) and GAPDH (1:2000) (Ward et al., 2013). After overnight incubation at 4°C and rinsing in TBS-T, membranes were reacted with IR Dye 800CW goat anti-mouse IgM (LI-COR, #925-32280) and IR Dye 680RD goat anti-rabbit IgG secondary antibodies and imaged as above.

Aggregation assays with tau biosensor cells

Transduction of tau biosensor cells with PBS-soluble brain extracts derived from tau transgenic mice was performed as previously described with minor modifications (Polanco et al., 2016). Cells were seeded 24 h prior to treatment with brain lysates in 12-well plates (Corning, #353043) at a density of $4x10^4$ cells/well. Cells to be analyzed by microscopy were grown on 18mm glass coverslips with a poly-D-lysine coating (Sigma, #P6407). Tau aggregation was initiated by adding 200μl OptiMEM (Life Technologies, #31985062) containing 2μg of protein in WT, rTg4510 and Tg/Fyn$^{-/-}$ PBS brain lysates, which was added dropwise to cells. The cells were then maintained in DMEM containing 1% FBS, without antibiotics, for 72 h until analysis by FRET flow cytometry and confocal microscopy.

FRET flow cytometry

FRET flow cytometry was performed with unmodified HEK293T, RD-CFP, RD-YFP, and tau biosensor RD-CFP+RD-YFP cell lines as previously described (Polanco et al., 2016). Cells were harvested with 0.25% trypsin-EDTA (Life Technologies, #25200056), fixed for 10 min with ice-cold 2% PFA and resuspended in HBSS containing 1mM EDTA. The FRET signal was quantified with a BD FACSAria cell sorter. To measure CFP and FRET-YFP, cells were excited by a 405nm laser (Coherent Inc.) and the emitted fluorescence was recorded at 485/22nm-filter and 530/30nm-filter, respectively. For each replicate, 40,000 events were quantified, and a gating strategy for eliminating doublets was used as outlined previously (Polanco et al., 2016). FRET data were quantified as an integrated FRET signal, which was calculated by multiplying the percentage of FRET-positive cells by the mean 530nm fluorescence intensity of the sample. Data, which were obtained from two replicate experiments, were analyzed using FlowJo xV software (Tree Star).

Microscopy of cells grown on coverslips

The cell medium was aspirated and PBS containing 1.23μg/ml Hoechst 33342 nuclear stain (Invitrogen, #62249) was applied for 25 min at room temperature. Cells were then rinsed once more in PBS and fixed for 20 min at room temperature in 4% PFA in PBS. After three brief washes in PBS, coverslips were mounted onto slides with Vectashield antifade fluorescent mounting medium (Vector, #H1000). Cells were imaged at 20x with a LSM710 scanning confocal fluorescence microscope (Zeiss).

Molecular cloning

pENTR vectors containing full-length (441aa) human tau and Y18E and Y18A point mutations were generated by site-directed mutagenesis using an in-house modified Q5 Site-Directed Mutagenesis kit (NEB, #E0554S). Tau constructs were further amplified by primers containing overhangs compatible with ligation-independent cloning (LIC). pET-His6-TEV-LIC vector 1B (Addgene #29653), a gift of Scott Gradia, was linearized by digestion with SspI-HF (NEB, #R3132S) and gel-purified. Tau inserts and linearized vector were treated with T4 DNA polymerase (NEB, #M0203S), annealed through LIC, and transformed into BL21(DE3) competent cells (NEB, #C2527I). Vectors were confirmed by sequencing prior to protein expression. All oligonucleotides were purchased from IDT.

Recombinant tau expression

Freshly picked colonies of BL21(DE3) containing hTau, Y18E and Y18A bacterial expression vectors were inoculated with vigorous shaking (275 RPM) overnight at 25°C in 50mL of Terrific Broth containing 55μg/ml kanamycin (AMRESCO, #0408-10G). One-liter cultures of Terrific Broth with 55μg/ml kanamycin were further inoculated with 15mL of overnight cultures, and upon reaching an OD600 of 0.6 (approximately 2 h) were induced with 0.5mM IPTG (Meridian Bioscience, #BIO-37036) and incubated with shaking (275 RPM) overnight at 25°C. Pellets were recovered by centrifugation and stored at −80°C until lysis.

Bacterial pellets were resuspended in lysis buffer (300mM KCl, 50mM KH_2PO_4, 5mM imidazole, pH 8.0) with Complete Mini Protease Inhibitors, 1mg/ml lysozyme (AMRESCO, #0663-10G) and 10U/ml Benzonase Nuclease (Sigma, # E1014). Cells were lyzed by intermittent sonication (Sonics Vibra-Cell VCX130, 60% amplitude) for a total of 3 min on ice and cleared by centrifugation at 25,000*g* for 30 min at 4°C. Lysates were filtered with a 0.22μm filter and His6-tagged proteins were purified with the use of an automated Profinia Protein Purification System (Bio-Rad). In brief, lysates were applied to Profinity IMAC resin columns (Bio-Rad, #7324610), washed with lysis buffer and wash buffer (lysis buffer with 10mM imidazole) and eluted with elution buffer (same buffer with 250mM imidazole). The eluate was then desalted using a Mini Bio-Gel P-6 Desalting Cartridge (Bio-Rad, #7324504) into physiological fibrillization buffer (10mM HEPES, 100mM NaCl, 1mM DTT, pH 7.4).

Proteins were concentrated to ~150μl with Amicon Ultra-4 30kDa MWCO centrifuge units (Millipore, #UFC803024) and further purified by size-exclusion chromatography using a Superdex 200 Increase 10/300 GL column (GE Healthcare, #28990944) with

an ÄKTApurifier chromatography system (GE Healthcare) in fibrillization buffer. A280 peak fractions were collected and assayed for tau expression by Coomassie/REVERT total protein staining and immunoblot with the anti-total-tau antibody Tau5. The same peak fractions were collected for each of the tau species assayed. Tau-containing fractions were concentrated as above, and the tau protein concentration was adjusted to 2mg/ml (~40μM) by measuring with a NanoDrop 2000 spectrophotometer (Thermo Fisher) using molar extinction coefficients (ε/1000) of 8.10 for non mutant hTau and 7.45 for Y18E and Y18A mutants, as calculated by the online ExPasy ProtParam portal (Gasteiger et al., 2005). Single-use aliquots were snap-frozen on dry ice and stored at −80°C until use in fibrillization assays.

Thioflavin T tau fibrillization assay

Eight micromolar of each tau species was mixed with 4μM heparin (Sigma, #H3393) and 10μM Thioflavin T (Sigma, #T3516) in fibrillization buffer (10mM HEPES, 100mM NaCl, 1mM DTT, pH 7.4), and 100μl volumes were added to black 96-well clear-bottom plates (Corning). Reactions were incubated at 37°C for 72 h in a CLARIOstar plate reader (BMG Labtech), and fluorescence was read every 5 min at an excitation of 440-10nm and emission of 480-20nm at a focal height of 4.2mm. For each 5 min cycle, the plate was shaken in a double-orbital fashion for 15 s. Experiments were performed in triplicate and performed three times. After the completion of the 72 h experiment, 30μl of each reaction was mixed diluted 10-fold in cold TBS, and then dot-blotted in triplicate for TOC1 as outlined above.

Image and immunoblot analysis

Immunohistochemistry and immunofluorescence slide scanner images were cropped to individual images and designated regions of interest (ROIs) corresponding to cortical and hippocampal subfields were manually drawn in ImageJ (FIJI). The percentage area of positive labeling was recorded for each ROI. A minimum of three ROIs for a given brain region were analyzed for each animal. For both DAB and fluorescence, the threshold for positive labeling was defined as the average value that excluded three standard deviations-worth (i.e., approximately 99.7%) of pixels according to the histograms of a minimum three positive control rTg4510 sections. Images were scored with a customized, automated macro, thereby negating the requirement for blinding. For fluorescence images, the macro was adapted to also measure the integrated fluorescence density.

Gallyas-stained sections were imaged as above and individual images were blinded. Silver-positive neurons were manually counted with ImageJ within three rectangular ROIs positioned semi-randomly in the neocortex. ROIs were kept identical in both size and orientation for each image. The average count across the three ROIs for each section was recorded.

Confocal images of tissue stained for glia were captured as a z stack of 78 images with a step size of 0.13μm, for a total depth of 10μm. Images were taken in the CA1 hippocampal region and processed in ImageJ by maximum z-projection followed by background subtraction and thresholding with the inbuilt Otsu threshold, and the percentage area of glia in each image was recorded.

Images of biosensor cells bearing tau aggregates were thresholded in the FRET-YFP channel and Hoechst/DAPI channels, generating binary masks for tau aggregates and nuclei respectively. The percentage area of aggregates, normalized to Hoechst/DAPI, was analyzed by ImageJ. For the analysis of aggregate morphology in FRET tau biosensor cells, blinded images were classified according to previously described prionoid tau aggregate morphologies (Sanders et al., 2014).

For immunoblots and dot-blots, the intensity of the main immunoreactive region of each lane was quantified with ImageStudio software (LI-COR). For immunoblots, values were normalized to REVERT total protein staining across all molecular weights. Dot-blots were normalized to GAPDH intensity in the case of mouse brain samples or to REVERT for ThioT aggregation assays. As the immunoreactivity of WT mouse brain samples in dot-blots and immunoblots for all anti-tau antibodies was negligible, they were excluded from graphs for additional clarity. Normalized data for rTg4510 and Tg/Fyn$^{-/-}$, reported as mean and standard error of the mean (SEM), were therefore represented as fold change relative to the rTg4510 results.

QUANTIFICATION AND STATISTICAL ANALYSIS

Unless otherwise stated, all n-values for animal experiments represent individual mice. Mice were assigned to treatment groups in a randomized fashion, whereas for cell culture experiments randomization was not required. Cell culture and *in vitro* experiments were replicated at least twice, with multiple technical replicates. All statistical tests were performed with Prism 8 software (GraphPad). Values are presented as mean ± SEM, with statistical significance being determined as *p* values generated with a 95% confidence interval, as indicated in the figure legends.

For behavioral and histological analyses, two-way ANOVA test with Tukey's multiple comparisons tests was initially performed to establish the presence of an interaction between gender and genotype. When no such interactions were discovered (data not shown), data were pooled by genotype, cleaned by Prism's inbuilt ROUT outlier identifier analysis (Q = 1%) (Motulsky and Brown, 2006), assessed by Shapiro-Wilk normality test and one- or two-way ANOVA (for behavioral analyses), Student's t test or nonparametric Mann-Whitney (for histological analyses) test were performed as required. For biochemical analyses and glial analyses, one-way ANOVA with Holm-Sidak's post hoc tests for multiple comparisons was used. The integrated FRET signal from flow cytometry was analyzed by either Student's t test or nonparametric Mann-Whitney test.

Kinetic data for ThioT reactions were calculated by fitting the data to a sigmoidal growth curve in Prism with the equation $Y = Y_{max}/1 + e^{-k(t-t1/2.)}$ (Lin et al., 2020). The parameters for the time of half-maximum aggregation ($t_{1/2}$) was extracted directly from model, and lag time (t_{lag}) was calculated with the equation $t_{lag} = t_{1/2} - (1/k)$ (please note this modified formula makes use of the approximation that $t_{1/2} \approx t_m$, where t_m is the x-coordinate with greatest growth rate) (Shoffner and Schnell, 2016). The area under the curve was calculated in Prism using the trapezoid rule, with the equation $\sum \Delta X \times (Y1 + Y2/2 - baseline)$. All data were plotted after normalization with respect to hTau.